(12) INTERNATIONAL APPLICATION PUBLISHED UNDER THE PATENT COOPERATION TREATY (PCT)

(19) World Intellectual Property Organization
International Bureau

(43) International Publication Date
30 October 2008 (30.10.2008)

PCT

(10) International Publication Number
WO 2008/128372 A1

(51) International Patent Classification:
G01N 21/31 (2006.01) *G01N 21/45* (2006.01)

(21) International Application Number:
PCT/CH2008/000178

(22) International Filing Date: 18 April 2008 (18.04.2008)

(25) Filing Language: English

(26) Publication Language: English

(30) Priority Data:
60/925,378 20 April 2007 (20.04.2007) US

(71) Applicant *(for all designated States except US)*: **ETH ZURICH** [CH/CH]; Raemistrasse 101/ETH transfer, CH-8092 Zurich (CH).

(72) Inventors; and
(75) Inventors/Applicants *(for US only)*: **BALMER, Tobias** [CH/CH]; Mattengasse 14, CH-8005 Zürich/ZH (CH). **HEUBERGER, Manfred** [CH/CH]; Rossweidstrasse 10b, CH-9030 Abtwil/SG (CH). **ZÜRCHER, Stefan** [CH/CH]; Starengasse 7, CH-8052 Zürich/ZH (CH).

(81) Designated States *(unless otherwise indicated, for every kind of national protection available)*: AE, AG, AL, AM, AO, AT, AU, AZ, BA, BB, BG, BH, BR, BW, BY, BZ, CA, CH, CN, CO, CR, CU, CZ, DE, DK, DM, DO, DZ, EC, EE, EG, ES, FI, GB, GD, GE, GH, GM, GT, HN, HR, HU, ID, IL, IN, IS, JP, KE, KG, KM, KN, KP, KR, KZ, LA, LC, LK, LR, LS, LT, LU, LY, MA, MD, ME, MG, MK, MN, MW, MX, MY, MZ, NA, NG, NI, NO, NZ, OM, PG, PH, PL, PT, RO, RS, RU, SC, SD, SE, SG, SK, SL, SM, SV, SY, TJ, TM, TN, TR, TT, TZ, UA, UG, US, UZ, VC, VN, ZA, ZM, ZW.

(84) Designated States *(unless otherwise indicated, for every kind of regional protection available)*: ARIPO (BW, GH, GM, KE, LS, MW, MZ, NA, SD, SL, SZ, TZ, UG, ZM, ZW), Eurasian (AM, AZ, BY, KG, KZ, MD, RU, TJ, TM), European (AT, BE, BG, CH, CY, CZ, DE, DK, EE, ES, FI, FR, GB, GR, HR, HU, IE, IS, IT, LT, LU, LV, MC, MT, NL, NO, PL, PT, RO, SE, SI, SK, TR), OAPI (BF, BJ, CF, CG, CI, CM, GA, GN, GQ, GW, ML, MR, NE, SN, TD, TG).

Published:
— *with international search report*

(54) **Title:** TRANSMISSION INTERFEROMETRIC ADSORPTION SENSOR

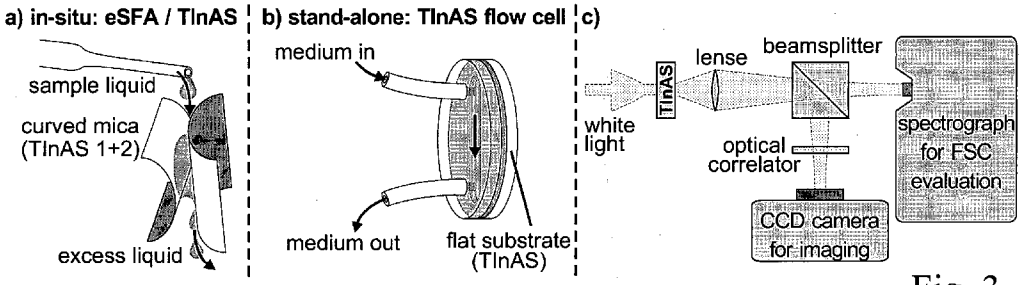

Fig. 3

(57) **Abstract:** A method and devices are presented for the measurement of adsorption based on thin-film interference at interfaces of a number of white light irradiated transparent layers, wherein the transparent layers have a total thickness of 2-100μm, wherein the secondary interference fringes resulting from the partial reflection of light at the optical interfaces, wherever the refractive index exhibits a discontinuity, wherein 5-100 secondary fringes are simultaneously analyzed and detected and used for the evaluation of the adsorption.

WO 2008/128372 A1

SPECIFICATION

TITLE

Transmission Interferometric Adsorption Sensor

TECHNICAL FIELD

The invention relates to methods and devices for the measurement of adsorption based on thin-film interference at optical interfaces of a number of white light irradiated transparent layers.

BACKGROUND OF THE INVENTION

The time-resolved measurement of molecular adsorption onto surfaces yields a wealth of valuable information about surface properties, solution properties, and adsorbent properties, adsorption mechanism as well as specific or unspecific adsorbent-surface interactions. It is for this reason that a number of different detection principles have been established to study molecular adsorption onto surfaces. These include label-free methods such as surface Plasmon resonance (SPR), waveguide or evanescent light techniques, interferometric systems, ellipsometry, quartz crystal microbalance, field-effect sensing, acoustic wave guiding, and, a host of molecular labeling techniques.

In contrast to the above mentioned adsorption onto a free surface, the direct forces between two such surfaces–decorated with adsorbed molecules–are highly relevant for studying intermolecular interactions. The extended surface forces apparatus (eSFA) is an established instrument based on the classical SFA that directly measures such surface forces. The change of thermodynamic free energy of interaction between two surfaces is measured as a function of surface distance. The in-situ combination of molecular adsorption- and direct force measurement opens new possibilities for the study of molecular interactions.

For practical reasons, a considerable effort is currently put into the development of new bio-sensors. Using surface patterning techniques, it has become possible to create multiple different adsorption spots onto a single surface. For future bio-sensor applications there is an increasing need for multi-spot analysis, or, surface imaging readout methods.

It is well known that the thickness of thin films can be measured in a Fabry-Perot interferometer, provided that the optical path, Ω, within the interferometer is a few tens of times greater

than λ/2, (λ wavelength used). For thinner films, a dielectric spacer layer is commonly used to adequately extend the optical path and facilitate the observation of interference effects. The thickness of a very thin film hence confined between or adsorbed onto such spacer layer(s) is then conveniently measured. A considerable number of experimental techniques are based on this principle.

For example, when monochromatic light of a sodium lamp is used to illuminate two glass slides in contact, one can readily observe interference patterns, so-called Newton rings. Newton rings are interference maxima that are located along lines of equal surface separation. They form the basis of several methods to image thin-film thickness. The simultaneous use of multiple colors has been envoked to improve the distance resolution to about ±1nm. The methods of highest resolution use white-light interferometry, where, the originally white light is color-modulated by passing through the thin-film interferometer and it is subsequently analyzed in a spectrograph. Such a transmission spectrum generally consists of multiple interference maxima – so-called fringes of equal chromatic order (FECO). The integer chromatic order, N=1, 2, 3... , is commonly used to designate the order of these interference maxima. In contrast to the 2D information obtained with Newton rings, the full-wavelength analysis using FECOs is, a priori, only one-dimensional (e.g. along a cross-section), but allows for a considerably improved thickness resolution (±0.1 nm). One spatial dimension of the image is eliminated by the Fourier transformation in the spectrograph. This dimensional reduction is at the gain of additional wavelength information comprised in the spectrograph exit plane. The cross-sectional geometry between curved mica crystals in the extended surface forces apparatus (eSFA) gives rise to the well-known characteristic shape of these FECOs. In the conventional SFA technique, wavelength-shifts of one chosen lead fringe (typically of odd chromatic order) is measured to analytically calculate film thickness and deduce the surface force.

SUMMARY OF THE INVENTION

In view of the above, the invention relates to and proposes different variants of a new molecular adsorption sensor based on Fabry-Pérot white light interference. The optional combination with spectral evaluation methods like fast spectral correlation (FSC) or optical spectral correlation (OSC), can be used to realize thickness measurements at high sampling rates and implement multiple spot analysis in scanning or imaging mode . Lastly, surface adsorption imaging with sub-second time resolution is demonstrated.

Figure 1a) shows the principal elements of the above-mentioned extended surface forces apparatus (eSFA). It essentially includes a substrate (optional but from practical considerations in most of the cases present), a mirror layer followed by a spacer layer and a gap medium. Essentially the same structure follows in the eSFA in the opposite order on the other side. The whole series of elements as given in figure 1a) is therefore necessary for an eSFA. This setup can be operated in transmission or reflection.

As will be detailed further below, the interference taking place between the mirror layers in the eSFA gives rise to the so-called primary interferences with sharp peaks (for an example see figure 1b). The relevant inter-layer distance for these primary interferences is designated with D(primary) and is the distance between the two mirror layers. For the primary interference fringes to be present, this distance D(primary) must be smaller than the correlation length of the irradiated light.

These primary interference peaks are used for evaluation in the eSFA.

As will also be detailed below, in addition to these primary interferences there are secondary interferences which are resulting from the partial reflection of light at optical interfaces wherever the refractive index exhibits a discontinuity. If the gap medium thickness (and correspondingly D(primary)) is increased beyond the correlation length of the irradiated light, or if one half of the structure as given in figure 1a is completely removed (for example removal of TInAS 2, so-called stand alone operation, optically equivalent to increasing the distance D(primary) beyond the correlation length of the irradiated light), the above-mentioned primary interference fringes disappear as there is no interference anymore between the two mirror layers. One such half structure is designated as TInAS, Transmission Interferometric Adsorption Sensor. Now the secondary interferences, resulting from the partial reflection of light at optical interfaces wherever the refractive index exhibits a discontinuity, and which were essentially masked by the primary interferences resulting from the mirror layers, now appear. These secondary interference fringes are used here if the total thickness of the transparent layers responsible for the secondary interference fringes (as determined by D(secondary) in figure 1a) is in the range of 2-100 micrometre.

The actual gist of the present invention is therefore the finding that the conventional eSFA setup can be modified for the measurement of adsorption (reflection or transmission measurements) by essentially using the above-mentioned secondary fringes only and eliminating the presence of primary interference fringes. This is possible by either completely removing one

half of the sensor (standalone sensor operation, e.g. TInAS 1 or TInAS 2 only) , or by increasing the distance between the mirror layers in an eSFA until the primary interference fringes disappear. In order to effectively be able to evaluate these secondary interference fringes with high accuracy, concomitantly a whole series of these secondary fringes is measured and evaluated for the determination of the properties of the adsorbed layer.

Specifically therefore, the present invention relates to a method for the measurement of adsorption based on thin-film interference at interfaces of a number of white light irradiated transparent layers. These transparent layers at least one of which is involved in the absorption process to be measured) have a total thickness of 2-100µm. The interference fringes of these transparent layers, resulting from the partial reflection of light at the optical interfaces wherever the refractive index exhibits a discontinuity, are measured as a stand alone sensor or under conditions such that the the gap medium thickness is larger than the light's correlation length. In addition, 5-100 secondary fringes are simultaneously analyzed and detected and used for the evaluation of the adsorption.

It is one of the key elements of the invention that specifically the peak wavelengths of the (secondary) interference fringes are measured which define the transparent layer total thickness which should be used, and, in contrast to the state-of-the-art, that not only one single interference fringe or signal is measured but a whole series of secondary fringes is simultaneously detected and used for the evaluation of the absorption properties within these transparent layers.

This (secondary) fringe pattern is, in accordance with a first embodiment of the invention, measured by using a CCD element, and preferably at least 10 pixels of this CCD element are illuminated by each interference fringe.

Generally, the shifts of the fringes are interpreted as thickness variation of a predetermined optical layer.

Different approaches are possible for the evaluation of the (secondary) fringes. According to one preferred embodiment, the simultaneously detected (secondary) fringes are evaluated using the fast spectral correlation (FSC) algorithm (for a detailed discussion see further below) either for single spot read out (for example using a pinhole aperture or a highly focused beam). The measurements can be carried out with a sampling rate of 10 Hz or more in these and the

other cases. The same algorithm can be used for sequential multi-spot read out by a scanning optics for laterally resolved measurements.

According to a further preferred embodiment, the light irradiated transparent layers include a spacer and a medium, and the difference in refractive index between the spacer and the medium is chosen to be larger than 0.1. Typically for the measurement of adsorption from aqueous media the spacer layer has a refractive index of at least 1.44, while for gaseous media the refractive index can be in the range **of 1.10-1.44 or greater**.

According to a still further embodiment of the invention, an optical spectral correlator (for a detailed description see further below) is inserted between the sensor with the white light irradiated transparent layers and the detector, the optical correlator transmitting only a selection of wavelengths and transforming the spectral information by the sample simultaneously into a laterally resolved greyscale image that is a direct measure for the laterally resolved adsorption layer thickness.

This optical spectral correlator can preferably be an optical multilayer etalon, preferably without adsorbed molecules. It can for example be based on at least one layer of cleaved mica with a thickness between 1.6 and 4.4 μm.

In particular if the above spectral correlator is used, the method can be carried out without any electronics and the device can be used as a portable, stand-alone device. In particular under these conditions it is possible that illumination is provided by daylight and the photometric detection is done with the human eye. In other words the sensor can be operated as a field device or it can for example also be integrated into other devices, it is for example possible to integrate such a sensor into glasses, sunglasses, windscreens, or the like e.g. for monitoring certain environmental properties (e.g. CO or O_3 content in the air or the like). Under these conditions the sensor does not necessitate the present of any electronics or power supply.

According to a preferred mode of operation, the transparent layers includes at least one solid layer and one liquid phase, wherein the the solid-liquid interface is typically the one, the changes of which are to be measured. Alternatively, in another mode of operation there is at least one solid layer and one gas phase, and here changes at the solid-gas interface due to adsorption of additional molecules is measured.

The proposed invention furthermore is related to a device which comprises a transmission interferometric adsorption sensor, which is for example based on 3-5 μm thick ruby mica sub-

strates, with the transparent layers as well as a spectrograph and/or an optical spectral correlator.

Preferred embodiment of this device is characterised in that the transmission interferometric adsorption sensor includes porous sensing layers with enhanced surface area such as porous materials or colloid beads, either on top of the transmission interferometric adsorption sensor, or, directly integrated into a spacer layer.

Is still further preferred embodiment of the device is characterised in that it further includes a source of white light and a beam splitter directing the transmitted light simultaneously to a spectrograph and an optical spectral correlator, as well as at least one CCD-element for the detection of transmitted light, wherein preferably the transmission interferometric adsorption sensor is given as part of a flow cell.

As already mentioned above, such a device can be a stand-alone element, either in the form of a microscope attachment or in the form of a device where the photometric detection is done with the human eye and the elimination is daylight.

In addition to the above, the present invention also relates to the use of the method or a device as described above for static and preferably dynamic/kinetic adsorption measurements selected from the group of: label-free true single molecule detection, study of interfacial phenomena such as adsorption to free surfaces or under confinement, preferably paralleled by direct force measurements for the study of phenomena of surface diffusion or structural forces in binary fluid systems in particular where one fluid forms a layer adjacent to the interfaces, sensing of multi-spot or large area bio-arrays, where not only the quantity of adsorbed mass on each spot is of interest, but also the adsorption kinetics, in particular for the study of adsorption from complex multi-component solutions, discriminating adsorbate molecules by adsorption kinetics, for example in diffusion limited adsorption, or, during adsorption under periodically varying conditions, measurement using conformational transitions of the adsorbate on the surface, measurement of condensation of thin liquid films from the vapor phase.

Further embodiments of the present invention are outlined in the dependent claims.

SHORT DESCRIPTION OF THE FIGURES

In the accompanying drawings preferred embodiments of the invention are shown in which:

Fig. 1 shows transmission interference in thin-film structures, wherein in (a) a schematic illustration of the typical thin-film interferometer is used in the eSFA; primary and secondary interferences can be distinguished according to the reflecting optical interfaces; in (b) typical interference spectrum is given showing primary fringes mainly due to multiple reflections between the mirror layers (e.g. Ag, Al) and in (c) a typical interference spectrum is shown consisting of secondary fringes as the result of partial reflections at optical interfaces, where the refractive index abruptly changes;

Fig. 2 shows the theoretical spectral contrast and wavelength shift of a TInAS as a function of refractive index differences, calculated for a 3μm spacer layer, which information is helpful for sensor design; wherein in (a) the spectral contrast for three common media (i.e. air, water, organic solvent) is plotted versus the refractive index of the sensor spacer layer; high spectral contrast is a key factor for precision peak detection; a minimum contrast occurs for index matching; wherein in (b) for the same three media the wavelength shift of the interference maxima for an ad-layer of 1nm (n_{ad}=1.5) is also calculated; the wavelength shift is a second important factor determining sensor sensitivity; interestingly, the wavelengths shifts are maximal for index matching conditions; optimal sensor design is thus around 0.1 index mismatch;

Fig. 3 shows an experimental setup for in-situ and stand-alone TInAS operation, wherein in (a) the thin-film interferometer inside the eSFA consists of two curved mica sheets, which are silvered on the outer faces; the gap medium can be a liquid (i.e. drop or submerged); in the point of closest approach (PCA) the surfaces are quasi parallel; each of the two multi-layer surfaces represents an individual TinAS; wherein in (b) the stand-alone TInAS generally consists of a multi-layered structure with a well defined surface against the fluid medium; and wherein in (c) the optical parts used for TInAS readout consist of a white light source, the interferometer (TInAS), an imaging lens, a beam-splitter as well as the spectrograph for single-spot readout with FSC evaluation, and, the OSC filter in conjunction with a photometric CCD camera for imaging TInAS readout;

Fig. 4 shows the adsorption of PLL-g-PEG copolymer from solution in-situ eSFA; this data illustrates a kinetic adsorption measurement with the TInAS (c.f. Fig 3a);

wherein in (a) the top graph adlayer thickness and adsorbed mass for a poly-cationic copolymer (poly-L-lysine-graft-poly-ethylene-glycol) from a buffer solution of 0.01mg/ml concentration, the sampling rate was ~1Hz and the spectra were evaluated using single-spot readout and fast spectral correlation (FSC) evaluation 15; wherein in (b) following to this measurement, the compression isotherm was measured with an eSFA loading/unloading cycle (c.f. Fig. 5); this type of measurement can yield detailed information about the molecular interactions and conformations of the adsorbed films on the surface of the sensor; this data illustrates the steric repulsion exerted by the PEG brushes after repeated adsorption of copolymer from solution;

Fig. 5 shows the stand-alone operation of the TInAS; adsorption of PLL-g-PEG copolymer from solution (0.1mg/ml) onto a substrate of SiO2; the copolymer was 50% functionalized with biotin; the adsorption was followed by buffer-rinsing to remove reversibly adsorbed copolymer, then followed by injection of neutravidin solution (20µg/ml) to provoke specific adsorption via biotin-neutravidin binding, followed by buffer to remove non-specifically adsorbed neutravidin; the data shows the excellent time resolution (sampling frequency ~1Hz) and the low noise conditions ~1Å; the adsorbed mass is reported on the right axis; it allows quantification of the number of neutravidin molecules specifically interacting with the biotin-functionalized surface; in this case we found that 7% of the biotin sites were involved in specific neutravidin binding;

Fig. 6 shows the detection of adsorbed water from the gas phase; stand-alone TInAS; the relative humidity was altered in stepwise manner as shown in the top part of the graph; the TInAS spacer layer was a thin sheet of mica; a 0.3nm film of water is found to reversibly adsorb onto the hydrophilic mica surface from humid atmosphere (RH=80%); N_2 purging of the experimental cell (RH=0%) contributes/leads to a reproducible desorption; the adsorbed water layer thickness is equivalent to only 1 molecular layer; the excellent signal-to-noise ratio in this TInAS experiment (resolution 5% of a monolayer) is a result of the relatively large difference in refractive index between the TInAS spacer layer (nmica=1.6) and the gas medium (n_{medium}=1.0) (see also Fig. 2);

Fig. 7 is a demonstration of scanning single-spot and imaging readout of TInAS; this series of images and graphs illustrates the scanning- and imaging readout options of the TInAS on a structured MAPL surface; the 60μm x 60μm squares are filled with 50% biotin functionalized PLL-g-PEG (c.f. Fig. 6) and the remaining surface is covered with un-functionalized PLL-g-PEG, which prevents unspecific protein adsorption; in (a): one-dimensional scan in single-spot readout mode; the data represent a cross section of the central MAPL square, before and after specific neutravidin adsorption; in (b): two-dimensional scanning of single-spot readout data measured across the same MAPL square after specific neutravidin adsorption; in (c): TInAS data measured in true imaging mode using optical spectral correlation; the image is taken on the same MAPL surface at the end of the adsorption of neutravidin; the remarkably low noise level (<1ng/cm^2) in this final image was obtained by averaging of 200 consecutive frames measured at ~2Hz sampling frequency; in (d): theoretical interference spectra of the interferometer and the OSC correlator used in the imaging TInAS data shown in (c);

Fig. 8 shows the principle of Optical Spectral Correlation (OSC): white light is directed through a thin film interferometer confining a film of variable thickness D(x,y) and refractive index n; the transmitted light is analyzed by a correlator and detected with a CCD camera; the overall transmitted light intensity is proportional to the spectral correlation function of the two transmission functions $T_{int}(D,n,\lambda)$ and $T_{corr}(\lambda)$ of the interferometer and the correlator respectively; the resulting correlation map I(x,y) yields laterally resolved, real-time information about the confined medium which then can be transformed into physical properties such as D and n; a computed example is given for a typical interferometer-correlator pair used in this work (mica = 4.3 μm, Ag layers = 40 nm, gap medium with n = 1.4); the correlation function shows a strong decay in intensity for D < 50 nm (true correlation); within that range the signal can be used for calibration; at larger gap distances higher order correlation maxima (false correlations) occur limiting the effective range of the method; the concentric ring structure seen in the correlation map is typical for the crossed-cylinder geometry of the interferometer used in the extended Surface Forces Apparatus (eSFA);

Fig. 9 shows design options for the optical correlator, wherein in (a): Calculated transmission function of an aluminum-coated correlator (Al-correlator: mica = 1.7 μm (1x), Al layer = 20 nm) compared to a silver-coated interferometer with twice the spacer thickness (Ag-interferometer: mica = 1.7 μm (2x), Ag layer = 30 nm); the interference maxima appear at the location of the odd-ordered fringes from the interferometer (bold black line); a slight rotation of the correlator results in a shift of the peaks towards smaller wavelength (grey lines); alternatively, a commercially available narrow bandpass filter can be used as simplified optical correlator (dotted line), in (b): Influence of the correlator-rotation on the shape of the OSC function; the region of highest sensitivity (slope) is shifted towards smaller gap distance; the inset shows a schematic of the two mica-correlator types; in (c): D-n correlation map of an Ag-interferometer in series with an Ag-correlator; the OSC function is sensitive to refractive index changes of the gap medium. (d) The n-sensitivity can largely be suppressed when using an Al-correlator;

Fig. 10 shows the performance of a CCD detector; the three major sources of noise are shot noise, read noise and dark noise; above a certain light level the shot noise becomes dominant and can be used to approximate the overall noise; calculations are based on the OSC camera used in this work (iXon, Andor Technology); with increasing signal intensity the relative error (noise/CCD signal) decreases until the pixels are saturated; high resolution OSC requires a relative error well below 1%. In our case, this is achieved for pixel saturation above 5%;

Fig. 11 shows the OSC calibration function and the theoretical film thickness resolution; the correlation function was calculated for a basic interferometer and a custom made Ag-correlator (mica = 4.3 μm, Ag layers = 40 nm, gap medium with n = 1.4); the resulting film thickness resolution was calculated according to Eq. 9 (fwc = 220'000 e-, nf = 1); sub-Å resolution is readily achieved with single exposure images; for a 9 x averaged signal the regime of sub-Å resolution is extended to nearly the entire distance range from 0 – 50 nm;

Fig. 12 shows performance data on OSC; wherein in (a): Normalized correlation function acquired with an Ag-correlator (mica = 4.37 μm) and the effective gap distance resolution calculated according Eq. 9 using fwc = 162'000 e-, nf = 1, NS = 1 (dashed line), 9 (dotted), 81 (grey); in (b): OSC signal at the PCA (Al-correlator)

in the regime of OMCTS layering transitions (bold black line); the signal is averaged over an area of 9x9 pixels i.e. an effective sample area of ~7x7 μm^2 from the interferometer; after photometric corrections the signal corresponds well to the independently measured gap distance with FSC (white circles); in (c): Characteristics of CCD signal noise plotted against the square-root of the mean intensity level; the noise from flat-field measurements at intensity levels above 5 % saturation (white circles) suggests a purely shot-noise dominated behavior as verified by a linear fit (bold black line); the effective OSC signal noise follows the same trend (grey line); this can be seen from an evaluation of the OSC signal inside an extended area around the PCA (c.f. inset) capturing the whole dynamic range of correlation intensities;

Fig. 13 shows examples of calibrated OSC data; wherein in (a): 3D-representation of the local contact geometry inside the interferometer of the eSFA; the data covers a region of 42x42 μm^2 and contains 3025 data points around the point of closest approach (PCA); a correlation map was acquired during isothermal compression of a thin film of OMCTS (bandpass correlator, 200 ms exposure) and subsequently translated into film thickness using the appropriate OSC calibration function; in (b): Evolution of the local contact radius as a function of the film thickness (at PCA); the radius is obtained by fitting a hemisphere to the 3D data points; the two lines result from two differently sized regions, acquired at 2 Hz during isothermal compression; the OSC measurement was paused between 2 and 3 nm (dashed lines); below 2 nm an OMCTS layering transition occurred; the mica surfaces used in this experiment were ~1.8 µm thick and glued to silica discs of R = 20 mm; and

Fig. 14 shows a comparison of the normalized transmitivity for different interferometer / correlator pairs; depending on the correlator type and the mirror coatings, the transmitted light level varies over two orders of magnitude; for fast measurements, i.e. high temporal resolution, a setup with high transmitivity is preferable; for example one can achieve sample rates of 20-30 Hz without significant loss of resolution using 30 nm silver coatings for the interferometer and correlator respectively (Ag30/Ag30); Ag = silver mirror, Al = aluminum mirror, BP = bandpass interference filter, the number indicates the corresponding thickness in nm.

DETAILED DESCRIPTION OF THE PREFERRED EMBODIMENTS

Referring to the drawings, which are for the purpose of illustrating the present preferred embodiments of the invention and not for the purpose of limiting the same, this document describes a high-speed adsorption sensor based on thin-film interference at interfaces. The sensor can be used as stand-alone instrument or in combination with a direct surface force measurement, which yields a wide range of additional information on molecular interactions on adsorbed films. The mass resolution of the presented method (± 1 ng/cm^2) is comparable to the one achieved in modern bio-sensors. The described method is suitable for the implementation of a low-cost bio-sensor with a minimal number of optical elements.

The measurement spot size is limited by the resolution of the imaging optics, typically in the order of one micrometer, and sampling rates >10Hz are readily possible. In contrast to other bio-sensors, the signal baseline has a remarkable long-term stability since the measured signal is virtually independent of refractive index changes in the fluid medium above the sensor surface.

In combination with the optional optical spectral correlation method, a label-free real-time imaging adsorption sensor can be realized. Sensor operation both inside the extended surface forces apparatus as well as in a stand-alone bio-sensor configuration is demonstrated in a first part. As an additional point, the imaging capability of this new sensor technology is illustrated on a patterned bio-functionalized surface.

<u>First part, general transmission interferometric adsorption sensor</u>

Theory: Let us consider a transparent dielectric multilayer structure, each layer exhibiting a different refractive index. Partial reflections at these optical interfaces lead to the formation and superposition of multiple beams–giving rise to an interference effect in the reflection- and transmission-spectra. Analysis of the resulting interference fringes can be used to determine small changes of film thickness, e.g. due to molecular adsorption. The experimental challenges of this method are the accurate wavelength calibration and accurate wavelength determination of the interference maxima. A considerable number of different instruments from various fields have been described that make use of the Fabry-Pérot or etalon multilayer configuration.

Primary and Secondary Interference Fringes in the eSFA: The cross-section of a Fabry-Pérot structure, typically used in the eSFA, is schematically shown in figure 1a. To enhance the finesse, two semi-transparent metallic layers are commonly evaporated as mirrors. These two

mirrors essentially define the outer boundaries of the interferometer; normally they are at a distance of 2-10 μm apart. In the eSFA, the gap medium is of variable thickness via a translation stage. The transmission spectrum of such etalon is dominated by the mirror-mirror reflections and consists of multiple narrow interference maxima as shown in figure 1b. This so-called primary fringe pattern exhibits a strong spectral intensity modulation Gamma=$(I_{max}-I_{min})/I_{max}\approx 90\%$. Primary fringes shift in wavelength when the distance between the mirrors is changed. Namely, when the thickness of one or multiple optical layers is varied; i.e. when the gap distance in the eSFA is increased they shift towards longer wavelengths. Measurement of these wavelength-shifts provides the very precise means for surface distance measurements used in the eSFA. The typical resolution is ±25pm.

In addition to the main reflection occurring at each of the mirrors, and independently therefrom, a partial reflection of light also occurs at the other optical interfaces; i.e. wherever the refractive index exhibits a discontinuity. A refractive index difference of 0.1 is usually sufficient to produce a measurable secondary interference contrast. As the gap medium thickness is increased beyond the light's correlation length, the primary interference pattern vanishes, whilst a secondary pattern becomes detectable. A typical set of such secondary fringes is shown in Fig 1c for the case of a back-silvered mica layer (e.g. $n_{mica}=1.59$) against an aqueous medium (e.g. $n_{water}=1.34$). Secondary fringes generally exhibit a smaller spectral modulation (e.g. Gamma≈25%) than their primary counterpart. In the presence of primary fringes, secondary fringes are thus barely noticeable as a faint background modulation.

It should be noted that the use of the term *secondary fringes* does not mean to imply that they are only present if also primary fringes are present. Quite in contrast, e.g. in the absence of mirrors only secondary fringes can be observed.

In the eSFA, a gap thickness of ≥200 μm is sufficient to detect the secondary pattern. Adjusting the focal plane, for example, to one of the half-interferometers minimizes the effective spot size on this surface, while the other surface contributes light from a larger area. Alternatively, it is also possible to use a confocal optical arrangement to analyze only one of the surfaces. In the eSFA, the former configuration is used.

It is important to note that the peak-wavelengths of secondary fringes are shifting upon the adsorption of molecules onto the surface–provided that these molecules have a different refractive index than the solvent medium from which they adsorb. This effect can be used to realize an in-situ molecular adsorption experiment. From the considerations presented above it

becomes clear that this Transmission Interferometric Adsorption Sensor (TInAS) can also be used as a stand-alone sensor technique outside the eSFA. In the following results section of the first part data for both incarnations of the TinAS are presented.

Sensitivity and sensor design: Most obviously, the TInAS sensitivity depends on the previously mentioned spectral intensity modulation. The limiting factor here is the change of refractive index from the spacer layer to the adjacent medium. This poses the boundary conditions for sensor design. In the limit of equal refractive indices of spacer layer and medium, no interference modulation can be made use of (Fig 2 a). The typical application of the TInAS involves adsorption of molecules from a given liquid solution directly onto a surface. A minimal difference of refractive index of typically approximately 0.1 between surface and medium, i.e. a spectral contrast modulation of Gamma = $(I_{max}-I_{min})/I_{max} \approx 15\%$, is required to obtain sufficient sensitivity. To measure in aqueous media, the spacer layer should have or must have a refractive index of 1.45 or higher. To measure adsorption from the gas phase, the signal will generally be much better.

In more detail, the experimental sensitivity achieved with a TInAS effectively depends on a number of factors. First, a strong spectral intensity modulation Gamma will facilitate the identification and wavelength measurement of the interference fringes (c.f. Fig. 2a). Second, the extent of the fringe wavelength shifts per adsorbate thickness will affect the spectral contrast. Third, the signal-to noise ratio is determined by factors like intensity variations, shot noise and detector noise. The dimensionless wavelength shift of the interference fringes per adlayer thickness change $\partial L/\partial D$ is used to compare the sensitivity of different sensor designs (c.f. Fig. 2 b). A higher refractive index contrast between the adsorbed adlayer and the medium will result in an increased sensitivity (Fig. 2c). Also, an increase of the spacer layer thickness will lead to a higher number of interference fringes that are simultaneously tracked (i.e. better statistics), however at the cost of a smaller wavelength shift per fringe. Figure 2a illustrates, for three different media, that the contrast factor has a minimum where the refractive index of the sensor equals that of the medium. In contrast, Figure 2b also shows that the peak shift per adsorbed thickness would be highest in precisely these situations. Due to these competing effects, there is no simple rule as to what refractive index of the sensor optimizes the sensitivity. Experience shows that a minimal difference of approximately 0.1 is a good basis. In any case, it is favorable to have a maximum refractive index difference between adsorbate and medium from which you adsorb (Figure 2c).

Conversion of thickness to adsorbed mass: The determination of the adsorbate thickness requires the correct input of the refractive index n_A of the adsorbing material. The resulting effective optical thickness D can readily be transformed into adsorbed mass, M, per unit area, which is a convenient physical quantity. We have the simple relationship $M = \rho \cdot D$ where ρ is the dry density of the adsorbate. Since adsorbates may remain partially solvated after adsorption, the density can be expressed in terms of the refractive index difference of the adsorbate, n_A, and the solvent, n_C, normalized to the concentration dependence of the refractive index in the mixture, dn/dc.

$$M = \frac{n_A - n_C}{dn/dc} \cdot D$$

For protein adsorbates, dn/dc = 0.182 cm^3/g is a reasonable value. The typical film-thickness resolution of the TInAS is better than ±20 pm, which translates into a nominal mass sensitivity of better than ±1 ng/cm^2. The exact resolution obtained in a given experiment depends on the parameters discussed in above.

The scanning single-spot readout of TinAS: To accomplish laterally resolved measurements, one has to analyze the transmission spectrum locally on the TInAS surface. The use of an objective lens is useful to project the image of the TInAS surface onto the (pinhole) aperture of a spectrometer. The sensitive diameter of this optical probe as well as the light intensity can be influenced by adjusting the lens and/or pinhole diameters. A lateral resolution of ~1μm at useful light levels is readily attainable. If the optical elements are designed such that lateral displacement in X and Y directions is possible, one can produce two-dimensional data sets by orthogonal scanning schemes. This multiple spot method has proofed to be useful in connection with patterned TInAS surfaces used as multi-functionalized arrays.

In practice, the evaluation of the measured transmission spectrum consists of two important steps, namely the detection and wavelength determination of the secondary interference fringes, followed by a numeric computation of the adsorbate thickness. In one proposed setup, the fringe detection is automated using a linear CCD. The wavelengths of the interference maxima are individually determined by the software. The result - an array of interference peak wavelengths - is then used to calculate the adsorbate thickness. For this numerical conversion the previously described Fast Spectral Correlation (FSC) algorithm is used (M. Heuberger,

Review of Scientific Instruments 72 (3), 1700 (2001)). FSC represents a limited inversion of the multilayer matrix theory.

The transmission spectrum of the bare sensor has to be determined prior to the adsorption experiment. This reference is used as optical zero. An arbitrary number of transparent layers with a total thickness of 2-100μm is admitted for the TInAS design. The number of simultaneously detected secondary fringes can vary in a wide range from 5-100. However, a minimum of ~10 pixels on the CCD should be illuminated by each interference fringe. These factors together determine an optimal choice of etalon dimension, spectrometer dispersion and detector resolution (e.g.CCD).

Imaging readout of TinAS: ways to exploit the localized spectral analysis for multi-spot scanning schemes have been described. To this end the use of an elegant spectral analysis that allows simultaneous and laterally resolved measurement of adlayer thickness at all points of the TInAS surface area–without the need of a scanning scheme-is described.

The lateral resolution (~1μm) of this imaging mode of operation is comparable or better than the scanning method described above, and, there is a considerable gain of measurement speed with this new approach—notably without a tradeoff in sensitivity.

As schematically shown in Figure 3 c, one can use an alternative optical path to illuminate a two-dimensional CCD camera for imaging purposes. The spectral analysis, which is normally done in a spectrograph, is realized via a special optical correlator that is simply inserted between the beam splitter and the CCD camera. The optical correlator, in connection with the CCD, transforms the spectral information transmitted by the TInAS into a grayscale image that is an unequivocal measure for adlayer thickness. The working principle of such optical spectral correlator (OSC) is described in detail in in the second part below. In summary, the optical spectral correlator is an optical multilayer structure comparable to the one used for the TInAS itself, but without adsorbed molecules, and, advantageously with a higher interferometric finesse. The optical spectral correlator is a color filter that only transmits a special selection of different wavelengths. The intensity of light transmitted through both elements in series, i.e. TInAS followed by the optical correlator, produces the wanted spectral correlation map (c.f. Figs 7c&7d). The optical spectral correlator can thus be seen as an optical element that calculates spectral correlation at all points of an image and therefore eliminates the need for the software-based FSC calculation. Since OSC relies on a photometric measurement rather than a spectroscopic one, a dispersive element (e.g. spectrograph) is no longer necessary, however, a

careful intensity calibration is now important if not essential to achieve data quantification. Common limitations associated with spectrograph calibration and peak detection are elegantly eliminated too, and, the calibration methods developed for OSC apply also for this variant of TInAS operation. The speed of measurement is no longer limited by computational power, rather by light intensity and CCD noise. Under optimal conditions the attainable resolution of adsorbed film thickness in aqueous solution is in the order of ±50pm on the entire image area with a lateral resolution of better than 5µm (±10pm for measurements in air). Common video frame rates are possible. The number of optical elements required is intriguingly small and cost-effective.

Experimantal setup, materials and results:

The main optical elements of a single-spot TInAS experiment are depicted in Figure 3c. White light is transmitted through the TInAS, which is alternatively located inside the extended surface forces apparatus (eSFA), or, used as stand-alone device in combination with a miniature flow cell. In the latter case, the flow cell is conveniently built on top of the flat sensor surface and connected to a tubing system that allows straightforward exchange of the medium. An aperture stop, such as a pinhole or an objective lens, is used to direct the transmitted light to the analyzing elements (spectrograph and CCD camera). Alternatively, an optical fiber may be used for this purpose (not shown). According to the two modes of operation, two alternative optical paths are illustrated in Figure 3. They can be used independently, or, in combination (beam splitter) and are each described separately:

The path for single-spot TInAS readout ends with a spectrometer (USB 2000, OceanOptics, USA) that digitally transmits the spectrum to a computer. Software is used to detect and determine the exact wavelength of the multiple interference maxima in the spectrum. The peak wavelengths hold the information about the adsorbed film thickness, which is extracted using the fast spectral correlation (FSC) method.

The imaging path consists of two principal elements: the optical correlator and a photometric image capturing device, e.g. calibrated CCD camera (iXon, Andor, Ireland). Intensity variations in the resulting correlation map are a direct measure for the adsorbed film thickness. A custom made interferometric filter can be used as correlator.

The TInAS used in this study were prepared from 3-5µm thick ruby mica substrates of high optical quality. Mica has the advantage that very clean and smooth surfaces can be readily

obtained by mechanical cleaving. To increase the finesse, a silver (30-50 nm) layer was evaporated onto one side of the TInAS by thermal evaporation at a nominal rate of 0.1nm/sec and a base pressure of $2*10^{-6}$ mbar. Alternatively, sputter coated sensors with 2-3 μm SiO_2 and 20-25 nm aluminum mirrors on a flat glass substrate were prepared to be used as stand-alone TInAS.

The flow cell used in the stand-alone sensors consists of three layers: the TInAS, an O-ring held by a template ring and, the transparent (e.g. polycarbonate) cover, which carries the inlet and outlet tubing. The template ring is a 1mm thick stainless steel disc with an oval 4.5x12mm opening in the middle to hold the O-ring (7x1mm) in place. The small fluid cell volume (~25μl) with its oval shape assures fast fluid exchange and uniform flow past the TInAS active surface area.

Adsorption tests were carried out from ultra-pure aqueous solutions, or, vapors thereof. For the adsorption results shown in Figures 4, poly-L-lysine-graft-poly-ethylene glycol copolymer with a grafting ratio of 2.9 and a PEG chain molecular mass of 5000 g/mol (PLL-*g(2.9)*-PEG(5)) was dissolved in aqueous buffer (10mM HEPES) solution at different copolymer concentrations. For the specific adsorption experiments in Figure 5 and 7, the copolymer architecture was functionalized such that every other PEG side chain carried a biotin receptor (50% PEG(2) and 50% PEGbio(3.4) with grafting ratio 3.5). The specific ligand was neutravidin dissolved in the same (10 or 150 mM) HEPES buffer solution than the functionalized copolymer. The temperature of all experiments was 22.5±0.5°C. The relative humidity (RH) inside the measuring chamber of the eSFA, or, the standalone flow cell was monitored with a CMOS sensor (SHTxx, Sensirion, Switzerland) and controllable to values between 0-90% via N_2/H_2O-bubbler mixing setup.

Results obtained with the TInAS under different operating conditions are described. It is started by an in-situ operation of two TInAS surfaces inside the extended surface forces apparatus. Therefore, a sub-monolayer of PLL-g-PEG copolymer was adsorbed onto two cylindrically curved mica surfaces inside the eSFA from a low concentration solution (0.01mg/ml). The two surfaces were separated by ~200μm. A droplet (~150 μl) of the aqueous medium was used here (c.f. Fig. 3a). The objective lens was re-focused to the gap mid-plane by a calibrated amount to collect the same amount of light from both surfaces. Figure 4a shows the temporal evolution of the TInAS signal expressed as film thickness [nm] or adsorbed mass [ng/cm^2], respectively. The first adsorption cycle was terminated after 70 minutes by rinsing the surfaces

with an excess of HEPES buffer. The surfaces were then brought into contact and a compression isotherm was measured in the eSFA. Figure 4b shows three different compression isotherms, obtained before and after different adsorption cycles. For SFA data evaluation, it is common practice to normalize the measured force, F, by the effective cylinder radius, R, and define positive values as repulsive forces. The second adsorption cycle was done in a solution of 10x higher concentration of PLL-g-PEG to further increase the polymer brush density at the surface. This gives rise to a longer range of the quasi exponential repulsion, also known as steric repulsion between the two surfaces decorated with polymer brushes. An increased range of repulsion is in agreement with theoretical expectations. A detailed evaluation of polymer brush conformation and steric repulsion observed with this system can be found in the literature. Analysis of TInAS data allows determination of some relevant quantities: Namely, the standard deviation of the TInAS signal (determined at saturation of the adsorption isotherm) is sigma=65pm at a sample rate of ~1 Hz. This corresponds to a sensitivity of the adsorbed mass of $\pm 4 ng/cm^2$. The total adsorbed mass can be calculated from knowledge of dn/dc (c.f. right scale).

Figure 5 shows data of a TInAS experiment carried out in a prototype of the stand-alone flow cell (c.f. Fig 3b). Here, the active TInAS multilayer was made of optical layers produced by Ar-plasma sputter coatings onto a flat glass substrate, starting with a 20 nm layer of aluminum followed by a ~2.5 μm thick layer of SiO_2. The flow cell used in this experiment had a particularly large volume of ~2.5 to produce diffusion-limited adsorption kinetics. After equilibration of the sensor in a 10 mM HEPES buffer solution we introduced 0.1mg/ml PLL-g-PEG(Bio50%), which is a PLL-g-PEG copolymer where every other PEG side chain is end-functionalized with a biotin receptor. The adsorption kinetics exhibits a fast initial adsorption with an asymptotic leveling thereafter. It is noted that all adsorbed mass is irreversibly adsorbed, i.e. no mass-loss upon rinsing. The second adsorption step was initiated by incubation with a dilute solution of 20μg/ml neutravidin, which can undergo a highly specific ligand binding reaction with the biotin already present on the surface. Analysis of the adsorption kinetics reveals that the final phase of the adsorption is diffusion limited (i.e. quasi-linear regime). The adsorption was stopped after 185 minutes by pumping HEPES buffer through the flow cell. Here too, the adsorption of neutravidin is irreversible on the timescale of the experiment. A very small increase of the signal after rinsing indicates that this large fluid cell volume was not completely exchanged with buffer and a small amount of neutravidin continues to adsorb while a slow surface rearrangement takes place. From the known adsorbed struc-

ture of PLL-g-PEG 20,21, the area per biotin in PLL-g-PEG(Bio50%) must be in the order of $6.5.10^{-14}$ cm^2. Comparison of the adsorbed mass before and after neutravidin incubation thus suggests that ≈7% of the biotin (244 Da) on the surface is bound to neutravidin (60 kDa).

The sensitivity of TInAS thus depends, among other factors, on the difference of refractive index at the sensor/medium interface. Until now, examples of adsorption experiments carried out in aqueous solutions are reported. For the reasons described above, the sensitivity of the TInAS is even higher in gaseous media. To demonstrate this effect, figure 6 displays data obtained with a mica sensor surface (n=1.6) in nitrogen gas (n=1.0). The molecular adsorbate is water from a nitrogen atmosphere of variable relative humidity. A very low relative humidity (0%) was obtained by flushing the flow cell with pure nitrogen. For the high relative humidity values (~85%), nitrogen was bubbled through a water reservoir prior to introduction into the flow cell. For the evaluation of this data, it is assumed that the adsorbed water layer had the same refractive index of bulk water (n=1.34). The top graph in Figure 6 records the alternating sequence of low and high relative humidity as a function of the elapsed time. The bottom graph displays the synchronously measured TInAS signal. One finds that a film of water is adsorbed that exhibits an optical thickness of ~0.35nm. Considering the oxygen-oxygen distance in bulk water (0.285nm), one can conclude that water does not appear to adsorb as a homogeneous monolayer. A more detailed TInAS study of the adsorption isotherm of water on mica from different media will be presented in a separate communication. Here it is focussed on the fact that the data in Figure 6 demonstrate the unprecedented signal to noise ratio in this experiment. It is in the order of ±12 pm (thickness), which corresponds to less than 5% of a water monolayer on the surface, or, an adsorbed mass sensitivity in the order of 1 ng/cm^2 — at a sampling rate of 2 Hz. It is also interesting to point out the remarkable stability of the TInAS baseline. In experiments similar to the above we observe effective drift of the baseline signal in the order of 1-2 Å (≈10ng/cm^2) over a period of 48 h. This is particularly useful for long-term adsorption/desorption experiments.

Modern bio-sensors require a fast measurement at multiple spots. As mentioned above, the TInAS single-spot operation can be extended with a scanning scheme, or, it can be operated as a real-time imaging sensor with µm lateral resolution. The entire sensor surface can simultaneously be read out by a CCD at video rates. A biotin-patterned TInAS surface can be used. A previously described MAPL-technique was used to structure the surface of a 3.7 µm thick mica sheet, which had a 50 nm silver mirror on the distant surface. The mica sheet was glued

on a supporting glass slide and used in combination with the above described flow cell design for the stand-alone TInAS (c.f. Fig. 3b). At that point, squares of 60μm x 60μm with 50% of the PEG side chains functionalized with biotin were present on the surface in a sea of protein-resistant PLL-g-PEG background. The 50% bio-functionalization inside the squares is, in fact, nominally identical to the one used for the experiment presented in Fig 5, where the entire surface, although being SiO_2, was homogeneously functionalized with PLL-g-PEG(Bio50%). The data shown in Figures 7a and 7b were obtained in multi-spot operation, i.e. by scanning of the TInAS single-spot optics and numerical evaluation of the transmission spectrum. As can be seen in the measurement before neutravidin incubation (Fig. 7a, open circles), the biotin functionalized squares exhibit a 0.15±0.05 nm thicker adsorbed film thickness. This small topographic effect is due to the additional length of the functionalized PEG chains (3.4 kDa) as compared to the non-functionalized chains (2 kDa).

After flushing of the patterned sensor surface with a buffer solution containing 20μg/ml of neutravidin for a few minutes, the adsorption of a 2.5±0.05 nm thick film is detected inside the square areas. A sequential spot scan of one selected square pattern is illustrated in Figure 7b. Analysis of the transition in the border region indicates a lateral resolution of ≤5μm with this imaging technique. A drawback of the sequential scanning method is the relatively long acquisition time. The high-resolution data shown in Figure 7b, which consists of 75 x 75 individual spot measurements, was acquired over an interval of 660 minutes.

The same TInAS was also imaged with an optical spectral correlator setup. A series of 180 frames (measured at 2 Hz) was averaged here to reduce the photometric noise to a level of ±1.2 Å per pixel. The nominal lateral resolution in this case is 0.76 pixels/μm. Figure 7c depicts the resulting grey image, which represents a correlation map carrying the information on film thickness. Brighter areas correspond to higher film thickness. A photometric calibration is needed to transform this correlation map into quantitative film-thickness information. The result is an accurate reproduction of the multi-spot profile shown in figure 7b, measured ~500x faster. The necessary calibration procedure is described in detail in a parallel communication 16. For illustration of the OSC principle, the corresponding spectra of the TInAS and the optical correlator, calculated for the given parameters, are shown together in figure 7d, where the adsorption of neutravidin leads to a small shift of the TInAS spectrum towards longer wavelengths. In series with the invariant correlator spectrum, the result is an increased intensity of transmitted light with adsorbed mass.

Discussion, first part

An issue of relevance for stand-alone operation is the roughness of the optical interfaces in the TInAS, particularly the roughness on the sensor surface. Since the interferometer presented here has a rather low finesse, the spectral modulation is limited and the interference modulation is rather broad. A roughness on a lateral sub-micron scale cannot be optically resolved and can thus lead to an additional broadening of the maxima. If the peak-to-peak roughness is less than some 10 nm, the operation of the TInAS is essentially unaffected. Features that laterally extend over distances larger than the optical resolution can be quantified as topographic information at sub-Ångström height resolution.

The TInAS noise level is determined by rather different mechanisms depending on whether fast spectral correlation (FSC) or optical spectral correlation (OSC) is used for readout. Since the latter method is realized with an optical calculation, the theoretical noise limit is determined by shot noise alone, which is a function of light-intensity. This parameter is independent of the number of adsorbed molecules, which means that label-free true single molecule detection should be possible with optical correlation readout.

In contrast to other adsorption sensors (e.g. SPR, OWLS), the TInAS is largely insensitive to changes of refractive index in the medium above the sensor surface. This results in excellent baseline stability. Together with the fast possible readout of >10Hz, the dynamic range of the TInAS is at least 4 orders of magnitude higher than that of other methods. For comparison, Fig. 15 lists a selection of important characteristics for common sensor types.

The combination of the in-situ TInAS inside the surface forces apparatus opens new ways of studying interfacial phenomena. It is possible to study adsorption to free surfaces or under confinement, paralleled by direct force measurements. Studying new phenomena of surface diffusion or structural forces in binary fluid systems becomes possible. In the later case one can distinguish different layers by their differences in refractive.

In terms of bio-sensing, the stand-alone TInAS can be seen as a low-cost variant with similar detection characteristics as the established sensors. However, based on its full frame imaging capabilities and largely increased dynamic range, new applications are conceivable.

For example, the TInAS may be used to sense multi-spot or large area bio-arrays, where not only the quantity of adsorbed mass on each spot is of interest, but also the adsorption kinetics. This can be of particular interest when adsorbing from complex multi-component solutions.

Discriminating adsorbate molecules by adsorption kinetics, for example in diffusion limited adsorption, or, during adsorption under periodically varying conditions (e.g. potential), or, using conformational transitions of the adsorbate on the surface, or, following long term rearrangements (e.g. Vroman effect) could be exploited to gain additional information.

Since the spectral contrast is enhanced in gaseous media, TInAS is an excellent sensor for adsorbates from the gas phase. A prominent example is the condensation of thin liquid films from the vapor phase. As demonstrated above, the sensitivity for water adsorption is comparable to the sensitivity of common vacuum techniques like X-ray photoelectron spectroscopy; e.g. <5% of a monolayer.

Other ways of achieving higher sensor sensitivity includes utilizing porous sensing layers with enhanced surface area (e.g. porous materials or colloid beads), either on top of the TInAS sensor, or, directly integrated into the spacer layer.

Using etalons instead of metallic mirrors could also help to increase the amount of transmitted light, or, increase the interferometer finesse at a particular wavelength. The TInAS can be designed to work in an optical correlation readout on a given wavelength regime and as window in another regime, which allows combination with other optical experiments, e.g. fluorescent labeling.

Since optical microscopes are readily equipped with CCD cameras and illumination, it is convenient to design the stand-alone TInAS in the form of a microscope attachment. For imaging applications the optical correlator can be designed as an integral part of the TInAS.

Last but not least, the TInAS can be used in applications where the photometric detection is done with the human eye and the illumination is simply daylight. In this latter case, the effective thickness of the adsorbed layer must be in the order of >50nm to see an effect. Contrast enhancement, for example, realized with high specific surface area layers or enhanced interferometer finesse can be utilized in this case.

Conclusions first part:

A new design and operation of a thin-film interferometric adsorption sensor (TInAS) based on the spectral correlation method is proposed. In connection with a numerical algorithm (fast spectral correlation) it is possible to realize a single-spot readout that can be extended to a sequential multi-spot readout by a scanning optics. Using an optical correlator in conjunction with a CCD camera (optical spectral correlation) an imaging mode of operation is also possi-

ble with typically 1μm lateral resolution. The sensitivity to adsorbed mass is in the order of 1-3 ng/cm^2 for all of above variants, and, thus comparable to other adsorption sensor types. The sensor exhibits a much higher baseline stability since it is not sensitive to changes of refractive index in the fluid phase above the sensor surface. Together with the comparably high sampling rates (>10Hz), the TInAS has a dynamic range that is 3-4 orders of magnitude larger than that of comparable devices.

Last but not least, the TInAS can be used as stand-alone instrument or, in-situ method during direct force measurements in the surface forces apparatus. This gives rise to numerous technical and scientific applications of this sensor technique.

Second part, film thickness imaging using Optical Spectral Correlation:

In this second part an optical method that allows one to measure the thickness and refractive index of very thin films in a typical thickness range of 1 nm to 50 nm in an imaging mode is presented as indicated above. Thereby, the transmitted light of a thin-film interferometer is spectrally correlated with a suitable optical element in its path. A CCD camera is used as the imaging photometer, yielding a laterally resolved correlation map, which can readily be transformed into the physical quantities (i.e. film thickness and film refractive index) of interest. To test the performance of this novel semi-quantitative method – Optical Spectral Correlation (OSC) –a modified setup of the extended Surface Forces Apparatus (eSFA) is utilized. Different options for the design of the correlator are presented. Furthermore, a detailed theoretical evaluation of the method's resolution based on a detailed signal-to-noise analysis, which reveals that a shot-noise dominated regime of operation is favourable is given. The predicted Sub-Å resolution is experimentally verified using data from single exposure-images, acquired at frame rates comparable to video standards (~25Hz). The procedures necessary to produce a reliable quantification of the OSC signal over the entire thickness range and image size are given. To illustrate the great potential of this new optical correlation method, OSC image data obtained in the eSFA with confined liquid films are discussed.

The use of a linear CCD array to acquire spectral information results only in a measurement at a point (Ø≈1μm), in contrast to the cross-sectional measurement described above. Lateral scanning of this optical probe at a point can, however, be used to obtain a three-dimensional representation of the film geometry in the contact region. Due to limitations in scanning speed (i.e. multiple CCD exposures and physical motion of optical elements), such a 3D acquisition may take several minutes to be completed.

This part describes optical spectral correlation (OSC) – a novel extension of the spectral correlation principle. Instead of the above described numerical FSC calculations, it uses an optical correlator to produce a two-dimensional, true-realtime image of the spectral correlation function. This image contains information on film thickness and film refractive index. The theoretical basis and the performance of OSC are described in detail. Furthermore, careful photometric calibration procedures are elaborated, which are advantageous for the technical implementation of this technique. The parameters relevant for system optimization as well as the implementation of OSC for the measurement of refractive index in ultra-thin films are discussed. The unprecedented resolution and the real-time imaging character of this new technique represent a valuable addition to the experimental assessment of ultra-thin film morphology and dynamics.

Theory: When white light is directed normally through a stack of stratified media, partial reflections occur at the optical interfaces. The amplitude of the reflected light and the associated phase change ϕ are a function of the complex refractive index, $\mu = n + ik$, on both sides of the optical interface. Multiple coherent beams of partially reflected light produce interference effects, depending on wavelength as well as the thicknesses of the optical layers. Constructive interference occurs if the total phase difference δ between successive rays passing back and forth is $\delta = 2\pi N$. The interference spectrum thus consists of multiple intensity maxima, each being associated with a different chromatic order, N. Variations of any film thickness or film refractive index result in wavelength shifts of these interference maxima – in analogy to a tunable resonator. If the thickness and refractive index of all but one layers is constant and known, measurement of these wavelength shifts can be utilized to determine changes of film thickness, D, and refractive index, n, of the one unknown (fluid) film between these spacer layers.

The transmission spectrum of a multi-layered thin-film interferometer can be predicted. Practically more useful in the context of the SFA technique is the reversed problem, namely the determination of D and n from a measured interference spectrum. Algorithms using fast spectral correlation (FSC, see reference given above) can considerably reduce the associated computational effort and allow for an expeditious (<100ms) conversion.

The Principle of Optical Spectral Correlation: Recent experimental progress has exposed a need for simultaneous measurement of film thickness and refractive index at all points within the contact area to assess the lateral distribution of non-equilibrium density fluctuations. Ide-

ally, one would wish for a real-time image showing the entire region of the confined fluid, while the information about D and n is encoded in the image at sufficient resolution.

To this end, the concept of optical spectral correlation (OSC) is introduced, which substitutes the above mentioned numerical calculation of spectral correlation by an optical calculator (Fig. 8). To this end, a special optical correlator (OSC filter) is designed with a transmission spectrum, $T_{corr}(\lambda)$, that corresponds to a reference spectrum (e.g. D=0) of the sample interferometer. When the two interferometers are placed in series, the intensity of the transmitted light, at any given point, corresponds to the product of the two transmission functions $T_{int}(D, n, \lambda)$ and $T_{corr}(\lambda)$. As a consequence, a maximum of light is transmitted at locations where the transmission spectra of both interferometers are identical. One can readily show that the total transmitted intensity $I(D, n, \lambda)$ is directly proportional to the spectral correlation function known from the numerical FSC calculations. When a white-light source is used, one can formally write:

$$I(D,n,\lambda) = \int_{\lambda} C(\lambda) \cdot T_1(D,n,\lambda) \cdot T_2(\lambda) \cdot d\lambda \qquad (1)$$

It is important to note that if the correlator spectrum consist of multiple maxima (e.g. FECOs), only the principal correlation (i.e. first correlation order) is the true correlation of high intensity. False correlations, i.e. FECO's of different chromatic order from the interferometer and the correlator coincide in their wavelengths, are significantly weaker. Note the underlying analogy to the numerically calculated correlation maps in the FSC.

With its power for parallel processing, the OSC method is optimally suited for real-time imaging applications. For detection, the light, which is transmitted through the sample interferometer and the optical correlator in series, is simply focused onto a CCD camera. The gray level image obtained directly corresponds to the spectral correlation map at any point across the area of interest. The main challenges of the OSC method lie in the design of the optical correlator as well as in the quantitative photometry using a CCD camera.

Design of the optical correlator: Typically the sample interferometer inside the SFA consists of two equally thick, back-silvered mica sheets mounted in a crossed-cylinder geometry with a lateral gap distance D(x,y). The most basic correlator would consist of a second set of identical mica sheets in a flat contact. With this setup the detected correlation map I(x,y) shows a concentric ring structure. The bottom part of Fig. 8 shows the calculated transmission functions (left) and the corresponding OSC function (right) of such a basic mica interferometer-

correlator pair. As expected, the highest OSC (true correlation) is obtained for film thicknesses near the reference; i.e. D(x)=0. Higher-order maxima of false spectral correlation exhibit considerably lower intensities. Such false correlations effectively limit the unambiguously detectable film-thickness range to about 50 nm. If we direct our attention to the true spectral correlation around D=0, we note that the intensity decays non-linearly depending on the refractive index (Fig. 9, c). It is the slope and shape of this intensity-decay that ultimately determine the resolution and the dynamic range of the OSC measurement.

There are several ways to customize the transmission function of the optical correlator in order to optimize detection range and sensitivity for a given OSC experiment. Basically, these are the parameters that affect shape and position of the correlator's transmitted FECO fringes.

The finesse, F, i.e. sharpness of the FECO, can be controlled by changing the reflectivity of the outer mirror surfaces. A higher mirror reflectivity generally leads to sharper peaks with a high peak-to-valley ratio. The reflectivity can be adjusted with the thickness of the mirror coating or with the selection of the mirror material. The finesse is the quantity that limits the slope and the range of the true correlation. For example, one can increase the OSC detection range by choosing thinner Ag mirror coatings; albeit at the cost of a reduced film thickness resolution (for a more quantitative calculus, see below).

The position of the interference maxima depends on the phase difference δ between two successive rays emerging from the interferometer. For the basic correlator design, with two spacer layers in direct contact, one has:

$$\delta_2 = \frac{4\pi}{\lambda}\mu 2T\cos(\theta) + 2\phi \qquad (2)$$

with T the thickness and μ the refractive index of the spacer, θ the angle of incidence and Φ the phase change on reflection at the mirror coating. Therefore, we can alter the fringe position by changing any of the parameters in Eq. (2). This corresponds to a tunable offset of the spectral correlation function against the film thickness. We can adjust the peak wavelengths of the correlator etalon spectrum by changing any of the parameters in Eq. (2). For example, one can tune the offset of the spectral correlation function relative to the molecular film thickness.

The magnitude of the phase change is given by the mirror material, and, for thin coatings it strongly depends on the mirror thickness. This allows to tune the position of the correlator peaks with respect to the interferometer spectrum, simply by adjusting the mirror properties.

Remarkably, this possibility can be utilized to design an interferometer-correlator pair with a resulting OSC function that is sensitive to D, but largely independent of n. For better illustration of this process let us consider the transmission function of a basic Ag-interferometer (i.e. two mica sheets of equal thickness in direct contact) as shown as gray area in the background of Figure 9 a). To build the correlator we use another piece of mica with identical thickness. If this piece of mica is coated with an Ag mirror on one side only, the phase increment within the correlator then corresponds exactly to half that of the interferometer, $\delta_{corr} = \delta_{\text{int}}/2$. The correlator FECOs selectively overlap with only the even-ordered FECOs of the interferometer. However, the correlator spectrum exhibits unfavorably low finesse in this case (i.e. broad peaks (not shown). In order to design a correlator with a higher finesse it is proposed to use aluminum mirrors on both sides of the mica piece (c.f. inset Fig. 9 b)). Here, one can make use of the natural coincidence that the phase changes of Al/mica and Ag/mica obey the condition $2\phi_{Al} \approx \phi_{Ag} + \pi$, and, therefore we can realize a high-finesse correlator with FECOs sufficiently near the position of the odd-odered interferometer FECOs. We note that in the presented case, the correlator fringe of order M overlaps with the interferometer fringe of even order N, where M=N/2. The additional phase change of $\Delta\phi=\pi$ from the correlator Al-mirrors is thus equivalent to a 2π-shift of the interferometer spectrum. Therefore, the correlator M-fringe is actually overlapping with the odd-ordered N+1 interferometer fringe. The theoretical spectrum of such an Al-correlator is shown in Figure 9 a) with a plain black line. For the basic interferometer used here one can show that odd-ordered fringes are not shifting when the refractive index in the film is varied, but the even-ordered fringes are shifting. Therefore, the Al-correlator is capable of analyzing film thickness independent of refractive index variations. For a better illustration of this property, the spectral correlation function is shown in Fig. 9d in the form of a two dimensional map in the Dn-plane. Figure 9 b illustrates that the spectral correlation function obtained with an Al-correlator has a maximum for a film thickness D~5-10 nm.

We now want to consider the effect of a correlator tilt angle with respect to the illumination axis. As shown in Eq. (2), the phase increment in a thin-film interferometer depends on the cosine of the incident light angle θ. One can use this effect to shift the correlator FECOs towards shorter wavelengths. This effect is small for angles below 2-3° and one can use this method to fine-tune the envelope of the OSC function. In particular it is possible to adjust the region of maximal distance resolution to a desired film thickness range. (for more details on resolution see below).

The preparation of customized thin-film correlators, as described above, can be rather involved. The use of a commercial interferometric bandpass-filter can be an alternative for less demanding applications. Such interferometric filters are available for a range of different central wavelengths and bandwidth. Once the thin-film interferometer is set up in the eSFA, one can chose an appropriate central wavelength to produce an overlap with a selected interferometer FECO. For interferometric bandpass-filters one can use the mentioned filter-tilting to fine-tune the wanted overlap. It is important to note that a custom-made OSC correlator will transmit considerably more light than a narrow bandpass filter because all FECOs can be used in the former case. Light intensity is indeed an issue of central importance in the technical implementation of OSC, since the measurement is essentially a quantitative photometric imaging problem.

Quantitative photometry using a CCD camera: The practical implementation of the OSC technique requires two steps: first, a quantitative photometric measurement, and, second followed by a calibration to transform the measured intensity into film thickness and/or refractive index. Considering the noise-to-signal ratio is essential for both steps since it determines the resolution of the OSC method.

The number of photoelectrons I_{e^-} that are generated when light falls onto a single pixel of a CCD detector can be expressed as

$$I_{e^-} = \eta \cdot I_{h\nu} = \eta \frac{\Phi}{h\nu} A \cdot t_{\exp} \tag{3}$$

That is the number of photons $I_{h\nu}$ times the quantum efficiency, η, of the detector, whereas each pixel of area A is exposed during the time, t_{exp}, to the light intensity Φ. Following exposure, the created charges are shifted to the read-out register of the CCD chip and are converted into digital A/D units, i.e. [ADUs] or [counts]

$$I_{ADUs} = G \cdot I_{e^-} = \frac{2^{\#bits}}{fwc} \cdot I_{e^-} \tag{4}$$

with G the electronic gain of the A/D converter and fwc, the full well capacity of each single pixel. The full well capacity is a measure for how many electrons can be created and temporarily stored on an individual CCD pixel before it saturates. Larger pixels have a higher fwc. It is convenient to normalize the intensity values by this saturation limit

$$I = \frac{I_{ADUs}}{2^{\#bits}} = \frac{I_{e^-}}{fwc} \quad (5)$$

The noise inherent to CCD exposure and signal processing effectively limits the resolution of the OSC method. Three sources of noise must be considered here, namely shot noise, read noise and dark noise. The shot-noise or photon-noise, σ_P, is a result of the quantum nature of light. The number of generated photoelectrons obeys Poisson's statistics and is therefore given by the square root of the total number of electrons. Read noise, σ_R, is mainly generated at the analog-to-digital conversion and increases non-linearly with readout speed. Faster data acquisition can only be performed at the cost of increased signal noise. High-end cameras offer the option to choose between different read speeds in a range of 1-10 MHz typically. There is an additional source of noise even in the absence of illumination or read-out action. It is the so called dark current, which originates from thermal fluctuations. The associated dark noise, σ_D, depends non-linearly on temperature and linearly on the exposure time. It can be strongly reduced by cooling the detector. Highly sensitive cameras therefore operate with cooled CCDs at temperatures as low as -90°C.

An additional source of noise arises at the signal amplifying stage of the camera in the form of a micro-channel plate (MCP) or a photo multiplier tube (PMT). This noise is inherent to the signal multiplying process and can be quantified by the so-called noise factor (nf), which multiplies the shot noise. The newer generation of CCDs is equipped with an on-chip electron multiplying (EM) device. Here, the charges are multiplied by impact ionization by passing through a biased gain register that is situated before the A/D conversion and signal amplifier. The result is an output signal for which the read noise becomes negligibly small19. The noise factor of EMCCD based devices is typically 1.4 whereas for other amplification techniques this quantity lies between 1.6 and 2.220.

Combining the noise sources above we can write an expression for the overall noise:

$$\sigma_{CCD} = \sqrt{\sigma_R^2 + \sigma_D^2 + nf \cdot \sigma_P^2} = \sqrt{\sigma_R^2 + \sigma_D^2 + (nf \cdot \sqrt{I_{e^-}})^2} \quad (6)$$

Where σ_R, is the read noise, σ_D, the dark noise and σ_P, the shot noise, nf is the noise factor, which depends on the CCD amplification technology. Fig. 10 shows a CCD operation chart, where the CCD signal and the corresponding noise is plotted as a function of the incoming light intensity. The data are based on the specifications of the iXon CCD detector used here. It

is important to stress that above a certain light level the overall noise is dominated by shot noise, which corresponds to the theoretical minimal noise. At the highest intensities we reach the pixel saturation level defined by the full well capacity. The relative signal error σ_{CCD}/I_{e^-} (top graph) is plotted against the relative pixel saturation. A low relative signal error can be achieved when working close to the pixel saturation. Under these conditions, a sufficiently high input light level is appropriate to reduce the exposure time and optimize for speed of measurement. In conclusion, a camera with a large full well capacity (i.e. large pixel size) and high quantum efficiency is favorable. If one aims for a relative OSC signal error better than 1%, one needs a pixel saturation of at least 5%. In this shot-noise-dominated regime of operation, the OSC signal noise can be approximated by

$$\sigma_{OSC}[e^-] = nf \cdot \sqrt{I_{e^-}} \quad \text{or as} \quad \sigma_{OSC}[rel] = nf \cdot \sqrt{\frac{I}{fwc}} \tag{7a,b}$$

Where I_{e^-} is the number of signal electrons and I the relative intensity according Eq. (5). The corresponding units are indicated within the brackets.

The resolution limit of OSC: The effective resolution, ΔD, that one can achieve in practice is limited by the measured OSC signal variation, ΔI, and the slope of the OSC calibration function as follows:

$$\frac{\Delta I}{\Delta D} \cong \left| \left(\frac{\partial I}{\partial D} \right) \right| \tag{8}$$

Using Eq. (7b) to estimate the signal variation, we get for the film-thickness resolution of OSC:

$$\Delta D = \frac{nf}{\left| (\partial I / \partial D) \right|} \cdot \sqrt{\frac{I}{N_S \cdot fwc}} \tag{9}$$

Fig. 11 shows this OSC resolution for a typical experiment. The regime of highest resolution coincides with the highest slope, $\left| (\partial I / \partial D) \right|$, of the OSC calibration function where one can readily achieve sub-Å resolution. In our example this is achieved in a distance range between 20-30 nm. In Eq. (9) we also introduced the number of CCD images, NS, used for averaging (i.e. noise reduction). Averaging can be implemented both by accumulating a series of single exposure images, or, by taking the sum from a cluster of neighboring pixels (binning). This

gain in film-thickness resolution is thus achieved either on the cost of time resolution or lateral resolution. In the example presented in Fig. 11, an averaging of NS = 9x (i.e. 3x3 pixel binning) would be sufficient to achieve a sub-Å resolution over a wide film-thickness range range.

Experimental Setup and Results

An experimental setup of the eSFA with simultaneous OSC and FSC capability was used. White light is directed perpendicularly through the sample interferometer inside the eSFA. A beamsplitter is used to simultaneously analyze the transmitted light with a spectrometer and a CCD camera. The spectrometer yields a localized quantification of the film thickness using (scanning) FSC. Behind the OSC correlator a CCD camera provides a laterally resolved, real time image of the contact zone inside the eSFA interferometer. Simultaneous operation of FSC and OSC allows for a direct calibration.

The FSC and OSC measurements described in here were obtained with a new variant of the extended Surface Forces Apparatus (eSFA). White light from a 450W Xe-arc lamp (Müller Elektronik Optik GMBH, Germany) is directed perpendicularly through the sample interferometer inside the fluid cell of the eSFA, from where it is focused on the pinhole aperture of a spectrograph and a CCD detector. We use a beamsplitter (Edmund Optics Inc., USA) to simultaneously operate in the FSC (i.e. spectrograph) and OSC (i.e. CCD camera) modes. The direct beam enters the spectrograph (USB2000, 385-715nm, Ocean Optics, USA) and is used for FSC measurement at a point. The spectrometer is mounted on a motorized xy-stage (Thorlabs Inc., USA) for lateral-scanning purposes. Special care was taken to minimize stray light using a series of aperture stops.

The indirect beam is directed through the OSC correlator before entering the CCD camera. The correlator is mounted on a rotational stage (home-built, positioning accuracy ±0.5 deg) with x'y'-alignment capability. The right choice of the CCD camera is important. It was done based on the considerations presented above. We are using an iXon DV887-BV from Andor Technology (Ireland). The CCD chip is a 512x512 pixel EMCCD sensor (CCD97-00, pixel size: 16x16 µm, typical full well capacity: 220'000 e-) made by e2V-Technologies. The specified quantum efficiency at 575nm is 92.5%. The frame transfer (FT) design of the CCD removes the need for a mechanical shutter. This is a great advantage when working with a vibration-sensitive technique such as the SFA. To reduce dark noise the CCD chip is Peltier-cooled to max. -90 °C. In addition, the CCD offers a choice of two output amplification modes, EM

and the conventional mode. The camera is capable of 14-bit resolution at pixel read out rates of 10*, 5*, 3 and 1 MHz (* only in EM mode). This allows for a frame rate of up to 32 Hz for full-frame transfer. Higher frame rates >100 Hz are possible with binning. According to the considerations above, the limiting parameter for speed is often the exposure time required to realize a measurement in the shot-noise dominated regime of operation. For the OSC data presented in this paper, we typically operated the camera at -50 °C in 3 MHz conventional amplification mode or at 10 MHz in EM mode (full frame) with exposure times ranging from 20 ms to 800 ms.

The thin-film interferometer inside the eSFA was prepared from sheets of cleaved mica with a typical thickness between 1.6 and 4.4 μm, following the standard protocol for sample preparation used in our lab. For the OSC correlator we used one (Al-correlator) or two (Ag-correlator) additional pieces of the same master piece (i.e. identical thickness). All mirror coatings were thermally evaporated at a base pressure of $< 4x10^{-6}$ mbar. Ag-correlators were prepared by bringing two back-silvered (typically 40 nm Ag) mica pieces into flat, direct contact. Al-correlators were made from a single piece of mica and coated separately on both sides with typically 20 nm Al. The optical correlators where then fixed in a custom-made aluminum frame. A clean filter area of a few mm^2 was sufficient for the OSC measurements. In some cases, an interference bandpass filter (λ = 532 nm, FWHM 3 nm, Edmund Optics Inc., USA) was used as optical correlator.

Octamethyl-cyclo-tetrasiloxane (OMCTS) was used as a model liquid for the eSFA / OSC demonstration measurements. This liquid is known to show characteristic layering transitions when confined between two smooth mica sheets.

In order to test the performance of OSC we conducted a series of thin film experiments with confined octamethyl-cyclo-tetrasiloxane (OMCTS). Spherical liquids like OMCTS are known to exhibit layering effects when confined to a few molecular diameters between atomically smooth mica surfaces. Due to the relatively large size of the molecule, the resulting oscillations in the free energy can be readily measured with the SFA. In a dry atmosphere, film-thickness transitions of stepsize ~9 Å are commonly observed below a film thickness of some 10 nm. Figure 12a shows an actual measurement of the OSC signal intensity (Ag-correlator), measured exactly at the point of closest approach (PCA) between two curved mica surfaces. A series of 125 data points was recorded while the mica surfaces were approached and the film thickness in the PCA was independently measured using the FSC method (X-axis). As ex-

pected from OSC theory, we observe a strong increase in the transmitted intensity below a gap distance of 50 nm (c.f. Fig. 8 and Fig. 11). The correlation peak is offset at D≈10 nm because mica is birefringent and the two sheets were not optically aligned. It can be shown that slightly misaligned mica in the Ag-correlator can cause such shifts. Another source of smaller shifts is the adsorption of molecular films of contaminants onto mica surfaces in the correlator, which may be different in the surface interferometer due to the different medium in contact with the surface. Adsorbed water or airborne hydrocarbons are potential candidates for adsorbed molecular films. Such an offset does not impair the OSC measurement and can readily be corrected for by using a modified calibration function. In the case presented in Figure 12, we could apply a polynomial fit of degree $7 \leq n \leq 13$, which could sufficiently well describe the OSC function. This function was then stored in a look-up table and used as the OSC calibration curve to transform the OSC signal into a gap distance.

We also carried out OSC experiments with other types of correlators such as the Al-correlator and the narrow bandpass filter. Furthermore, tilting of the correlator between 0 and 12 degrees was routinely used to tune the effective range and region of highest resolution. For the study of structural forces in OMCTS, the range of interest lies between $0 < D < 30$ nm, in particular below 10 nm where molecular-layering transitions are typically observed. The main difference between the three correlator types was found to be the total light level, which ultimately limits the system performance (i.e. resolution, speed). The highest OSC intensities could be realized with the Ag-correlator, followed by the bandpass and the Al-correlator (c.f. Fig. 14). Due to the higher absorption coefficient of aluminum, Al-correlators (40 nm mirrors) transmit less than 1/1000 of the light transmitted by an Ag-correlator with the same mirror thickness. Reducing the mirror thickness of the Al-correlator allows for useful imaging rates (~1 Hz), albeit at a reduced resolution (~5 Å). Fig. 12 b) displays the normalized OSC signal analyzed by an Al-correlator in the regime of OMCTS layering transitions (black bold line). The step-like change in intensity coincides with the layering transitions observed in the independent FSC measurement. The normalization of the OSC signal by the intensity of the light source was necessary to compensate for inherent small fluctuations of our Xe-arc light. Details on the light normalization procedures are given in the discussion section.

To quantify the experimental resolution of our OSC setup, an in-depth assessment of the CCD detector signal noise was carried out. From flat field intensity measurements at different levels

between 5-95 % of saturation, we find the following empirical behavior for the camera's conventional amplifier mode (3 MHz readout):

$$\sigma_{CCD}[ADUs] = 0.318 \cdot \sqrt{I_{ADUs}} \qquad (10)$$

This power law is indeed expected for a shot-noise-dominated mode of operation. Inserting Eq. (4) into Eq. (7) and comparing it with Eq. (10), one can estimate the actual full well capacity of our system. We find fwc = 162'000 electrons. This value is about 25% lower than the nominal value specified by the manufacturer. In a second step we acquired a series of OSC images with the interferometer surfaces in intimate contact. This series of 150 images was used to determine the mean and the standard deviation for each pixel. The analysis was done on the image area shown as inset in Fig. 12c, which contains the full scale of correlation intensities up to the first maximum of the true correlation. The result of this assessment is depicted in Figure 12c. There is good agreement between the noise behavior of the OSC signal and the flat-field noise of the CCD detector, which is purely shot-noise dominated. The additional scattering of the OSC noise data points is essentially due to the relatively low number of samples (150 samples for a given pixel and intensity) as compared to the flat-field averaging (full frame with 262'144 pixels at equal intensity).

It is thus reasonable to use this shot-noise analysis as a basis to quantify the OSC resolution in terms of film thickness. To this end we will use Eq. (9) and insert the actual full well capacity of the detector. Considering the measured OSC calibration function of the Ag-correlator (Figure 12a) we can indeed achieve sub-Å resolution for film thickness (one sigma) for each individual pixel of the CCD. The effective range of sub-Å resolution can be greatly extended if pixel averaging (e.g. binning) is used as shown in Fig. 12a. For example, with a super pixel of 3x3 CCD pixels we thus achieve a film thickness resolution well below 100 pm over a range of ~40 nm and still maintain a lateral resolution of 2-3 μm.

The ultimate strength of OSC is to allow for a fast, precise and accurate measurement of molecular film thickness in an entire region. Two examples of these remarkable capabilities are illustrated in Figures 12a and b. The top graph shows a quantified 3D-representation of the film thickness in the contact zone of the eSFA. A number of 3025 data points are shown in an area of 42x42 μm. The OSC calibration function (c.f. Figures 11a and 12a) was used to transform intensity into film thickness. This data was acquired with an exposure time of 200 ms, which allows a sample rate of 5 Hz. This is a 36'000x gain of measurement speed compared to

the same data acquired by the conventional scanning of the FSC probe – notably, at no loss of resolution. Using OSC, it is now possible to follow the entire contact geometry during an eSFA experiment. We have fitted a hemi-sphere into the type of data shown in Figure 13a to get a simple measure of the local radius R of curvature. Surface force measurements are commonly presented normalized to the local radius of curvature because this is a measure of the free energy at the interface (Derjaguin approximation). Figure 12b shows the evolution of the local radius of curvature during an isothermal compression of a thin fluid film of OMCTS. Two different curves are shown that correspond to a hemi-sphere fitted to an 31x31 μm and 41x41 μm area, respectively. We observe a local flattening of the surfaces due to repulsive surface forces. The curve of higher values corresponds to the more localized measurement, typical for contact flattening. The relative change of radius is more than 10% for the last 8 nm of the compressed liquid layer. As a control measurement, the 3D-scan by conventional FSC (ROI: 50x50 μm, 25x25 data points), taken prior to the isothermal compression at a gap distance of 340 nm, resulted in a radius of R = 20.5 mm.

Discussion: Reliable photometric field measurement lies at the heart of the OSC method. For convenience, we would like to divide this experimental problem into three parts, namely the flat-field correction, the lamp normalization and the OSC calibration (quantification). Followed by a section discussing the temporal resolution for dynamic measurement.

The flat-field correction: Real OSC images are prone to image irregularities and imperfections due to the 10+ optical layers the light has to pass. A closely related issue is the direct and homogeneous field illumination of the image area by the lamp, which is depending on design, geometry and unwanted reflections or scattered light. Furthermore, the pixels of a CCD detector all have an individual photosensitivity and individual dark noise characteristics. While some of these effects can be minimized (e.g. aperture stops, CCD cooling), the high accuracy of the OSC measurements calls for a flat-field correction of the following type:

$$I_{i,j} = \frac{(S_{i,j} - DF_{i,j})}{(FF_{i,j} - DF_{i,j})} \cdot \overline{M} \qquad (11)$$

where I(i,j) is the corrected intensity image (pixel indices i, j) as calculated based on the measured CCD signal S(i,j). DF is the dark frame containing the detector background (dark current integral and A/D-offset), FF the flat field reference image and $\overline{M}$ the background corrected average intensity of the flat field image, $\overline{M} = \overline{(FF - DF)}$. It is an important detail to note that

the exposure times of all images S, DF, and FF should be the same for the correction to work. In addition, the frames DF and FF are "noise-reduced" images obtained by averaging a large number of such exposures. The dark frame is easily acquired by darkening the CCD (e.g. shutter). It is however not trivial to obtain a representative flat field image with all the optical elements in place (i.e. with OSC modulations already in the image). To reduce the influence of such OSC modulations one can separate the interferometer surfaces to a large gap distance > 100 μm where the correlation modulation is far from the true primary correlation maximum and thus of smaller intensity. The drawback to this method is that at least one of the surfaces needs to be moved out of focus and therefore the resulting reference image is not truly representing the same flat field as during the OSC measurement. A better alternative is to keep the surfaces closer than ~1 μm and move the surfaces at constant speed (e.g. 5 nm/s) while accumulating a large series of OSC images. If a suitable sequence of images is averaged, the OSC modulations are averaged out and one obtains the wanted flat image F. Typically, the sample surfaces are moving over a range of separations of a few 100 nm during this procedure.

The lamp normalization : A control experiment revealed that a Xe-arc lamp can exhibit intensity fluctuations of around 5%, often irregular and over a time interval of several seconds. Presumably, these fluctuations stem from intrinsic arc instabilities. Since we aim for OSC measurements with a stability of better than 1% over an hour, we have to account for these effects. A simple possibility is to measure the lamp intensity with an independent photo sensor and mathematically normalize the measured OSC images. A more elegant way is to project a small fraction of the lamp light directly onto a dedicated section of the CCD detector. This can be realized, for example, by an optical fiber bypass or an optical aperture in the interferometer and correlator mirrors. The advantage of this approach is an automatic synchronization with the OSC exposure time.

Here, we want to describe a third method that uses the annular light from the first false correlation (secondary correlation), which occurs at somewhat larger film thickness ~150nm. To get a reliable measure for the lamp intensity, we fitted an elliptical contour to the secondary correlation maximum and averaged a fixed number of pixel values. One can extract the synchronized and noise-reduced reference intensity from each OSC image. An example is shown in the inset of Fig. 12c, dashed line. The center of this ellipse is conveniently used to define the location of the PCA. The data presented in Fig. 12b was normalized with this method. The normalized OSC signal is stable and perfectly reproduces the film thickness transitions inde-

pendently measured using FSC signal. The ellipsoidal contour fit of the secondary correlation has to be repeated for each image frame and is therefore more suited as an offline procedure.

The OSC calibration (quantification): Finally, the corrected and normalized photometric OSC intensity has to be transformed into film thickness. The possibility to carry out simultaneous OSC and FSC measurements is the great advantage of the proposed setup and is used here to establish an absolute, quantitative OSC calibration based on the absolute reference provided by FSC film thickness measurements. Notably, one can readily obtain an in-situ calibration, which automatically accounts for all systematic photometric deviations between theory and the actual setup. To this end, we describe the steps necessary to determine the effective OSC function, which is subsequently used to translate OSC images into film-thickness maps.

First, it is appropriate to assure the temporal and lateral coincidence between the two measurements (i.e. OSC and FSC). The temporal coincidence is provided by the computer using synchronized data acquisition. The lateral coincidence is based on an accurate determination of the PCA as the reference point: The alignment of the FSC probe to the PCA is a standard procedure in our laboratory and utilizes the lateral-scanning ability of the eSFA. To determine the location of the PCA in an OSC image, an ellipse is fitted to the second order correlation band of the OSC map as described above. Both methods can reproduce the position of the PCA with an accuracy of better 1 micron.

Second, the calibration is obtained by simultaneously measuring film thickness (FSC) and light intensity (OSC) for a relevant range of different film thickness. This could be done by varying the surface separation in the eSFA with the approach motor. As an alternative to such dynamic calibration we propose a static calibration procedure for which the two surfaces are brought into contact. A noise-reduced OSC image is acquired simultaneously with a lateral FSC scan across the contact zone. Finally the two data sets are plotted against each other to obtain the OSC calibration function. This method requires that the OSC detector is well aligned (i.e. rotation) and laterally calibrated in the xy-directions.

The OSC calibration has a limited lifetime, if, for example, the optical parts of the OSC setup undergo lateral drift. However, repeated calibrations obtained with an Ag-correlator suggest a sufficient stability for at least 1 h of measurement. For extended experiments at sub-Angstrom resolution, a periodic update of the calibration is recommended.

Dynamic Measurements: As mentioned in the results section the main difference between the three correlator types used in this second part (Ag-correlator, Al-correlator and bandpass-correlator) is the transmitted light intensity. This is of importance for experiments that require a high temporal resolution. In Fig. 14 we compare the normalized intensity level of the true correlation for different interferometer-correlator pairs. Depending on the correlator type and the applied mirror thickness the light level varies within two orders of magnitude. By far the highest transmitivity is obtained with 30 nm silver coatings on the interferometer and correlator respectively. With that setup we achieve frame rates of 20-30 Hz with full frame images (3 MHz readout) and without significant loss of film thickness resolution. For fast measurements the sample rate can also be increased by making use of the binning ability of our CCD camera.

Conclusions second part: In conclusion, one can show the usefulness of a novel optical spectral correlation method to image film thickness in real time at sub-Ångstrom resolution over a thickness range from 1-40 nm. The OSC method is based on the use of custom optical correlators. The presented OSC method allows measurements of dynamic effects occurring in molecularly confined films and brings unprecedented experimental capabilities to the extended surface forces apparatus.

CLAIMS

1. Method for the measurement of adsorption based on thin-film interference at interfaces of a number of white light irradiated transparent layers, wherein the transparent layers have a total thickness of 2-100μm, wherein the interference fringes of these layers, resulting from the partial reflection of light at the optical interfaces wherever the refractive index exhibits a discontinuity, are measured as a stand alone sensor or under conditions such that the the gap medium thickness is larger than the light's correlation length, and wherein 5-100 secondary fringes are simultaneously analyzed and detected and used for the evaluation of the adsorption.

2. Method according to claim 1, wherein the transparent layers include at least one solid layer and one liquid layer, or at least one solid layer and one layer of the gas phase, and wherein preferably changes at the solid-liquid interface or the solid-gas interface due to adsorption of additional molecules is measured.

3. Method according to any of the preceding claims, wherein the the transparent layers include porous sensing layers, preferably with enhanced surface area, such as porous materials or colloid beads.

4. Method according to claim 1, wherein the secondary fringe pattern is measured by using a CCD element, wherein the shifts of the fringes are interpreted as thickness variation of a predetermined optical layer.

5. Method according to claim 4, wherein the simultaneously detected secondary fringes are evaluated using a fast spectral correlation (FSC) algorithm either for single spot read out, preferably with a sampling rate of greater than 1 Hz or greater than 10 Hz, or for sequential multi-spot read out by a scanning optics for laterally resolved measurements.

6. Method according to any of the preceding claims, wherein an optical spectral correlator is inserted between the sensor with the white light irradiated transparent layers and the detector, the optical correlator transmitting only a selection of wavelengths and transforming the spectral information by the sample simultaneously into a laterally resolved grey-scale image that is a direct measure for the laterally resolved adsorption layer thickness.

7. Method according to claim 6, wherein the optical spectral correlator is an optical multi-layer etalon without adsorbed molecules, preferably based on at least one layer of cleaved mica with a thickness between 1.6 and 4.4 μm or between 3 and 5 μm.

8. Method according to any of the preceding claims, wherein illumination is provided by daylight.

9. Method according to any of the preceding claims, wherein the photometric detection is done with the human eye.

10. Method according to any of the preceding claims, wherein it is carried out as stand-alone sensor in combination with a miniature flow cell, wherein preferably the flow cell is build on top of a flat sensor surface and connected to a tubing system that allows exchange of a medium.

11. Method according to any of the preceding claims, wherein the stand-alone sensor is used as a microscope attachment.

12. Device for carrying out a method according to any of the preceding claims, wherein it comprises a transmission interferometric adsorption sensor, preferably based on 3-5 μm thick ruby mica substrates, with the transparent layers as well as a spectrograph and/or an optical spectral correlator.

13. Device according to claim 12, wherein the transmission interferometric adsorption sensor includes porous sensing layers with enhanced surface area such as porous materials or colloid beads, either on top of the transmission interferometric adsorption sensor, or, directly integrated into a spacer layer

14. Device according to claim 12 or 13, further including a source of white light and a beam splitter directing the transmitted light simultaneously to a spectrograph and an optical spectral correlator, as well as at least one CCD-element for the detection of transmitted light, and wherein preferably the transmission interferometric adsorption sensor is part of a flow cell.

15. Device according to claim 12 or 13, wherein it is a stand-alone element, either in the form of a microscope attachment or in the form of a device where the photometric detection is done with the human eye and/or the illumination is daylight.

16. Use of the method according to one of claims 1-11 or of a device according to any of

claims 12-15 for static and preferably dynamic/kinetic measurements selected from the group of: label-free true single molecule detection, study of interfacial phenomena such as adsorption to free surfaces or under confinement, preferably paralleled by direct force measurements for the study of phenomena of surface diffusion or structural forces in binary fluid systems in particular where one fluid forms a layer adjacent to the interfaces, sensing of multi-spot or large area bio-arrays, where not only the quantity of adsorbed mass on each spot is of interest, but also the adsorption kinetics, in particular for the study of adsorption from complex multi-component solutions, discriminating adsorbate molecules by adsorption kinetics, for example in diffusion limited adsorption, or, during adsorption under periodically varying conditions, measurement using conformational transitions of the adsorbate on the surface, measurement of condensation of thin liquid films from the vapor phase.

17. Use according to claim 16, wherein the measurement is an adsorption kineticsmeasurement.

18. Use according to any of claims16 or 17, in combination with surface forces measurements.

Fig. 1

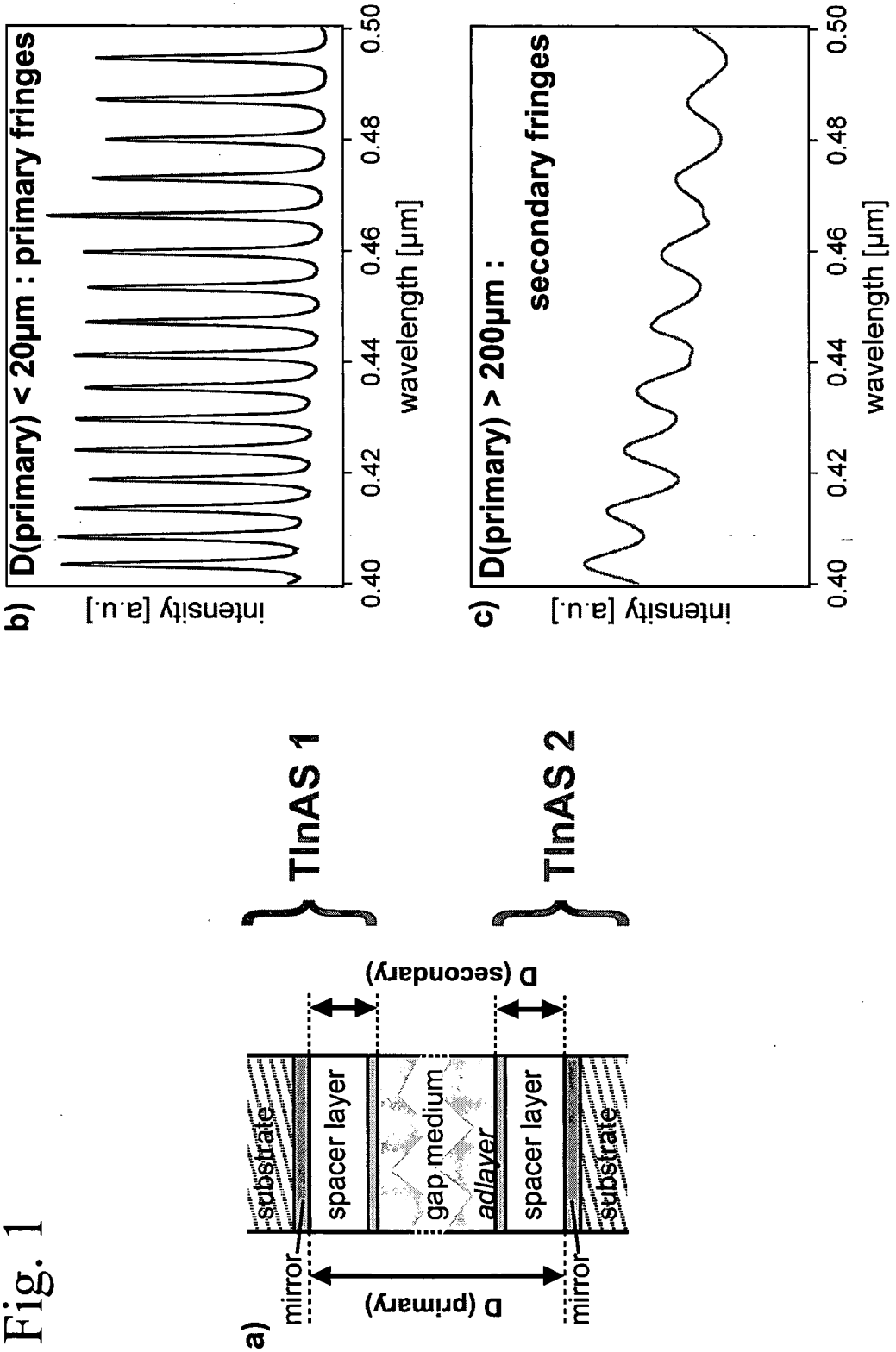
a)
mirror
substrate
spacer layer
gap medium
adlayer
spacer layer
substrate
mirror
D (primary)
D (secondary)
TInAS 1
TInAS 2
b)
D(primary) < 20µm : primary fringes
intensity [a.u.]
0.40
0.42
0.44
0.46
0.48
0.50
wavelength [µm]
c)
D(primary) > 200µm :
secondary fringes
intensity [a.u.]
0.40
0.42
0.44
0.46
0.48
0.50
wavelength [µm]

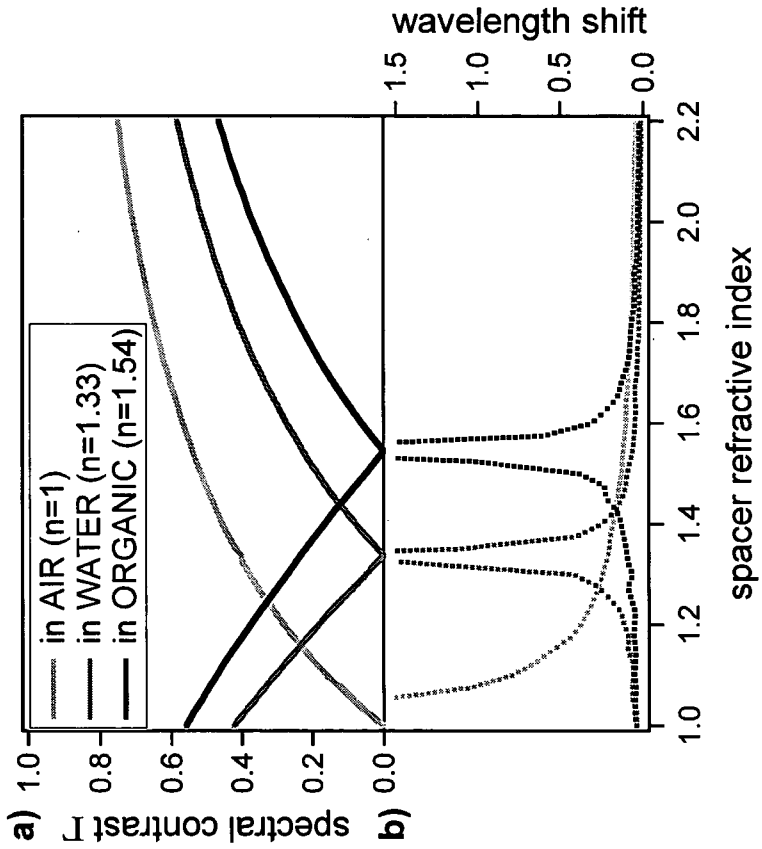
wavelength shift
1.5
1.0
0.5
0.0
in AIR (n=1)
in WATER (n=1.33)
in ORGANIC (n=1.54)
1.0
0.8
0.6
0.4
0.2
0.0
a) spectral contrast Γ
b)
1.0
1.2
1.4
1.6
1.8
2.0
2.2
spacer refractive index

Fig. 2

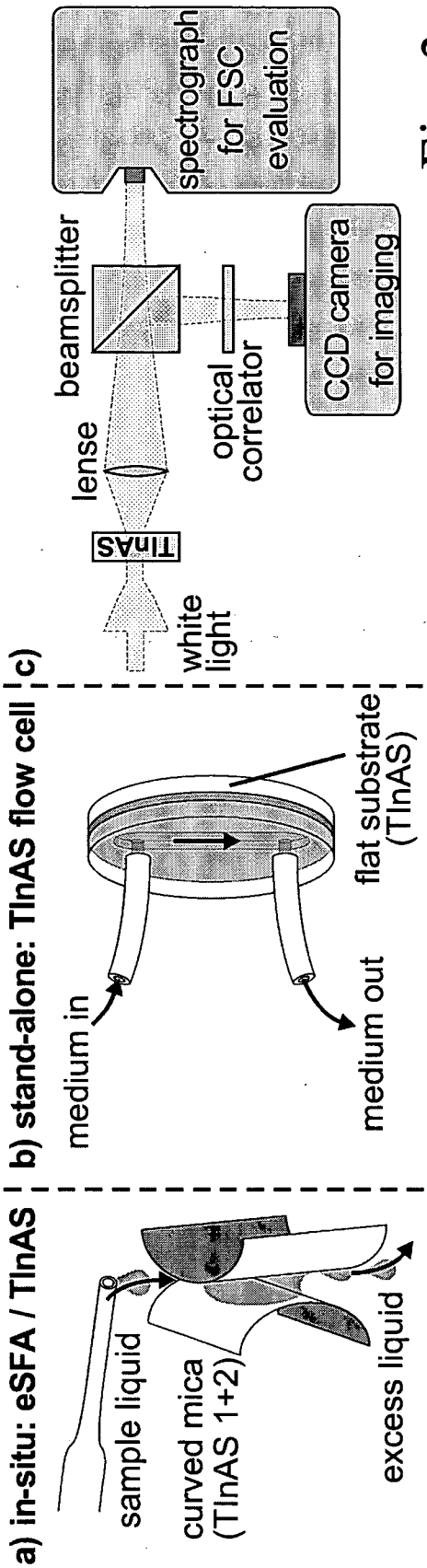
a) in-situ: eSFA / TInAS
b) stand-alone: TInAS flow cell
c)
sample liquid
curved mica
(TInAS 1+2)
excess liquid
medium in
medium out
flat substrate
(TInAS)
white
light
TInAS
lense
beamsplitter
optical
correlator
CCD camera
for imaging
spectrograph
for FSC
evaluation

Fig. 3

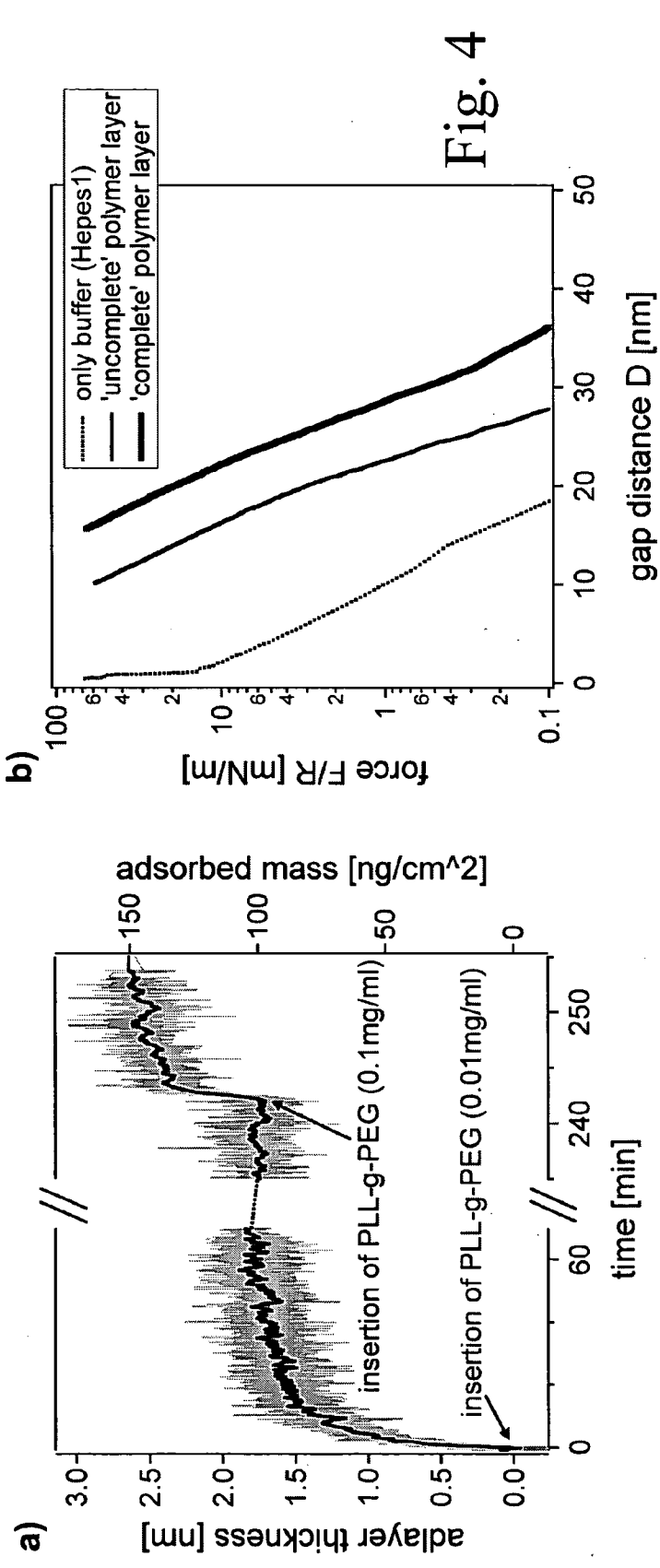
a)
adlayer thickness [nm]
adsorbed mass [ng/cm^2]
time [min]
insertion of PLL-g-PEG (0.01mg/ml)
insertion of PLL-g-PEG (0.1mg/ml)
b)
force F/R [mN/m]
gap distance D [nm]
only buffer (Hepes1)
'uncomplete' polymer layer
'complete' polymer layer

Fig. 4

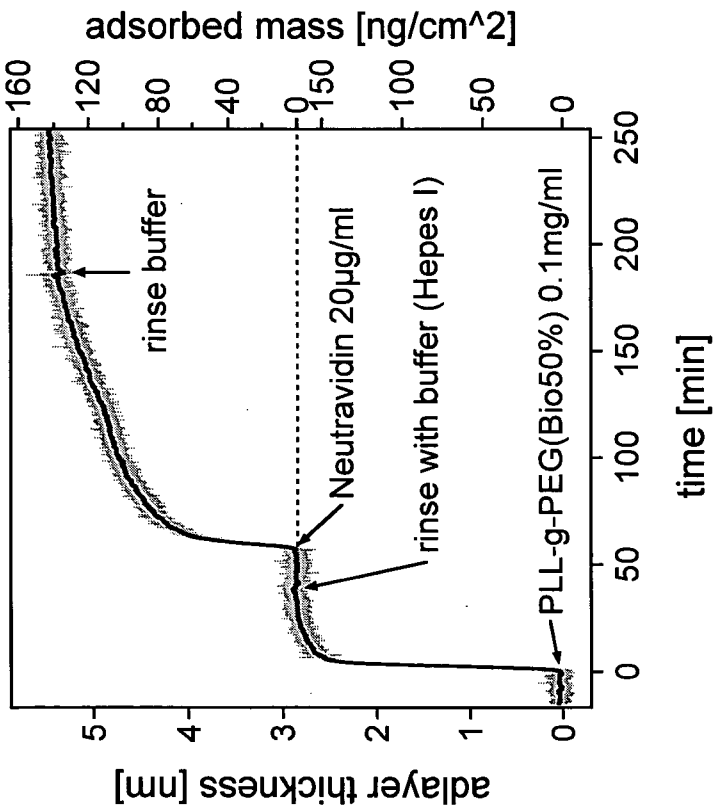
adsorbed mass [ng/cm^2]
160
120
80
40
0
150
100
50
0
rinse buffer
Neutravidin 20µg/ml
rinse with buffer (Hepes I)
PLL-g-PEG(Bio50%) 0.1mg/ml
0
50
100
150
200
250
time [min]
adlayer thickness [nm]
5
4
3
2
1
0

Fig. 5

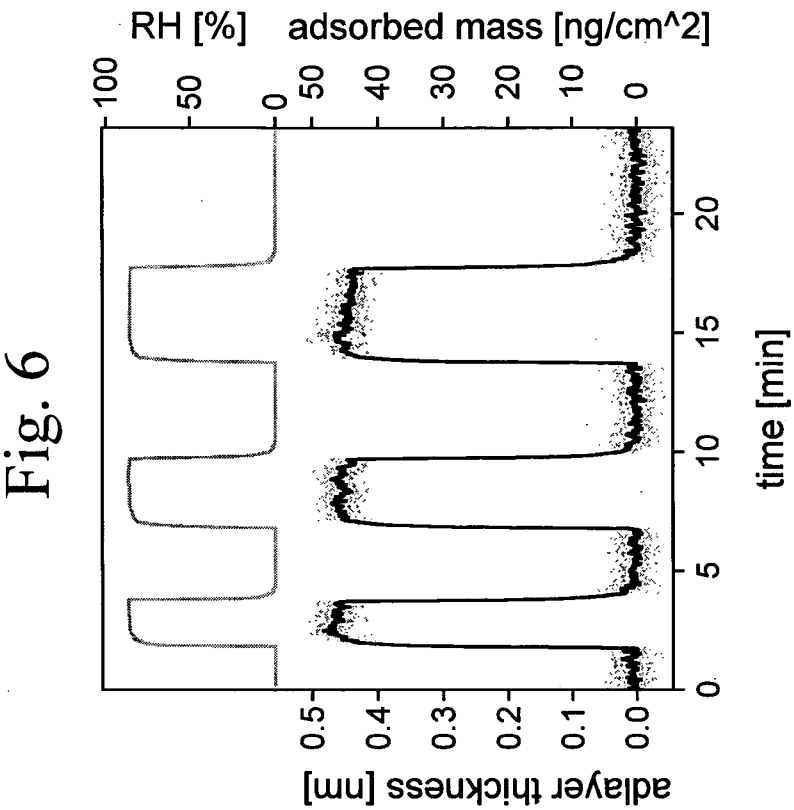
RH [%]
adsorbed mass [ng/cm^2]
100
50
0
50
40
30
20
10
0
0
5
10
15
20
time [min]
adlayer thickness [nm]
0.5
0.4
0.3
0.2
0.1
0.0

Fig. 6

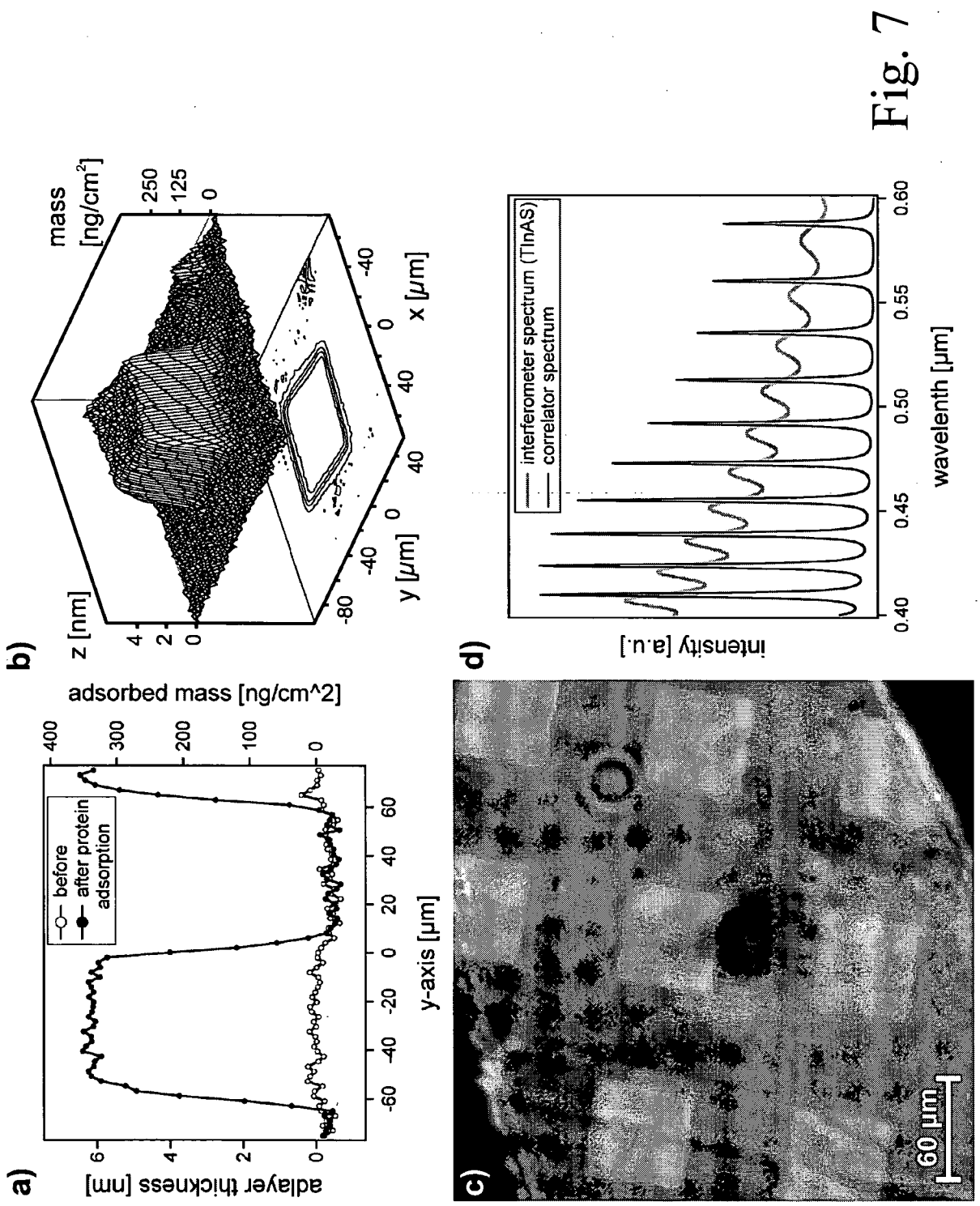
a)
adlayer thickness [nm]
y-axis [µm]
before
after protein adsorption
adsorbed mass [ng/cm^2]
b)
z [nm]
y [µm]
x [µm]
mass [ng/cm²]
c)
60 µm
d)
intensity [a.u.]
wavelenth [µm]
interferometer spectrum (TInAS)
correlator spectrum

Fig. 7

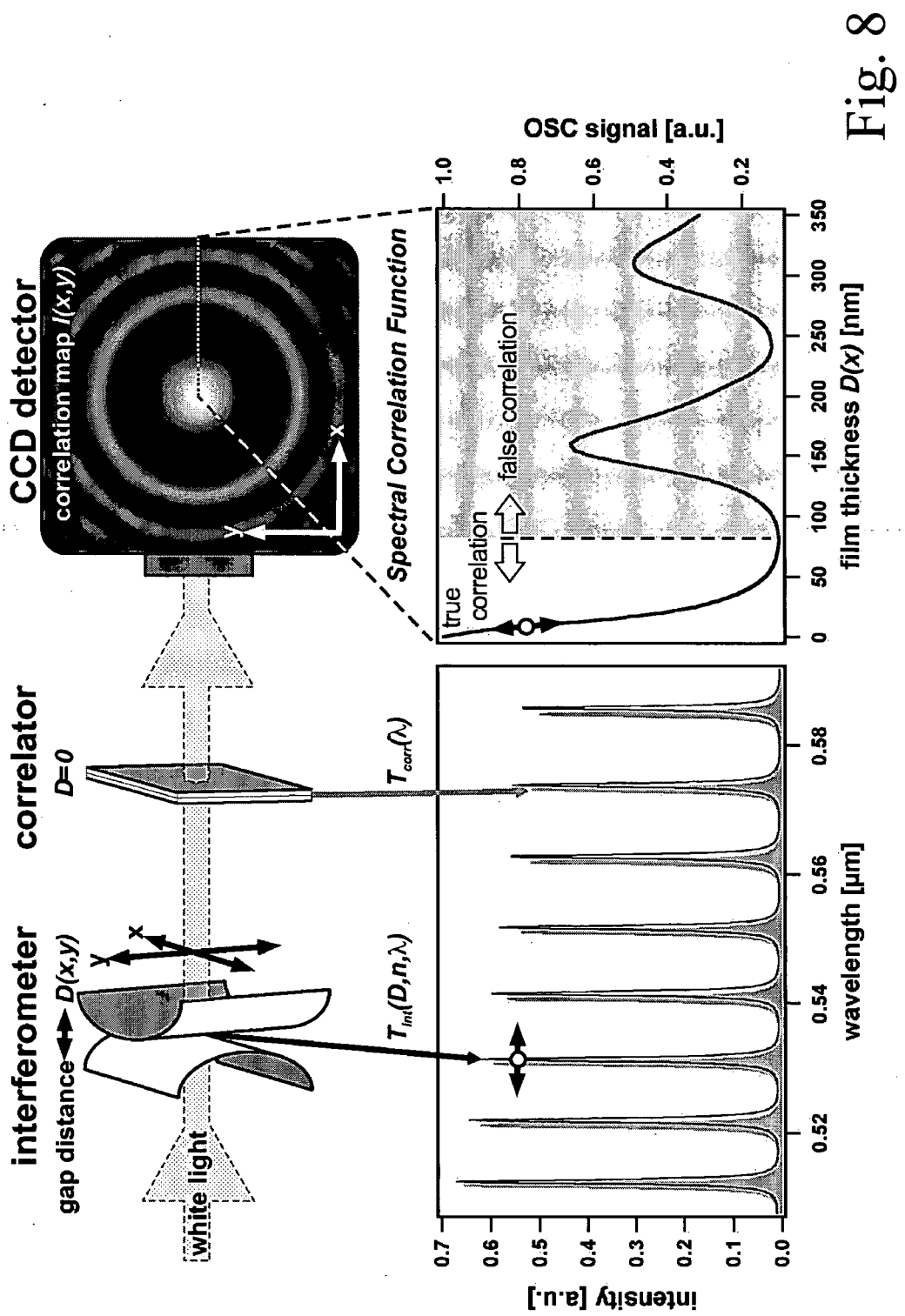
CCD detector
correlation map I(x,y)
Spectral Correlation Function
OSC signal [a.u.]
1.0
0.8
0.6
0.4
0.2
true correlation
false correlation
0
50
100
150
200
250
300
350
film thickness D(x) [nm]
correlator
D=0
T_corr(λ)
interferometer
gap distance D(x,y)
T_int(D,n,λ)
white light
intensity [a.u.]
0.7
0.6
0.5
0.4
0.3
0.2
0.1
0.0
0.52
0.54
0.56
0.58
wavelength [µm]

Fig. 8

Fig. 9

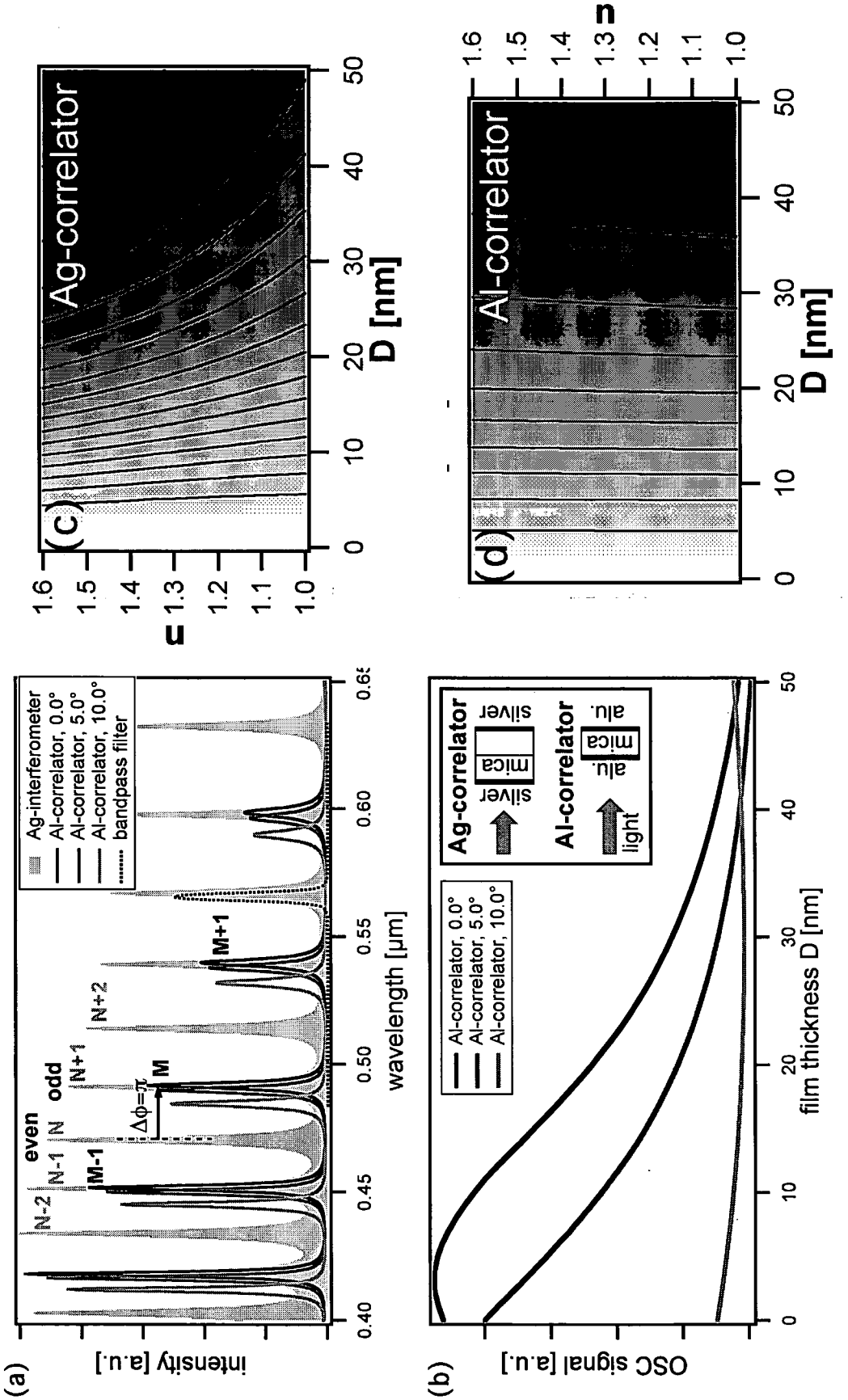
(a)
intensity [a.u.]
wavelength [µm]
Ag-interferometer
Al-correlator, 0.0°
Al-correlator, 5.0°
Al-correlator, 10.0°
bandpass filter
even
odd
N-2
N-1
N
N+1
N+2
M-1
M
M+1
Δφ=π
(b)
OSC signal [a.u.]
film thickness D [nm]
Al-correlator, 0.0°
Al-correlator, 5.0°
Al-correlator, 10.0°
Ag-correlator
silver
mica
Al-correlator
alu.
mica
light
(c)
Ag-correlator
n
D [nm]
(d)
Al-correlator
n
D [nm]

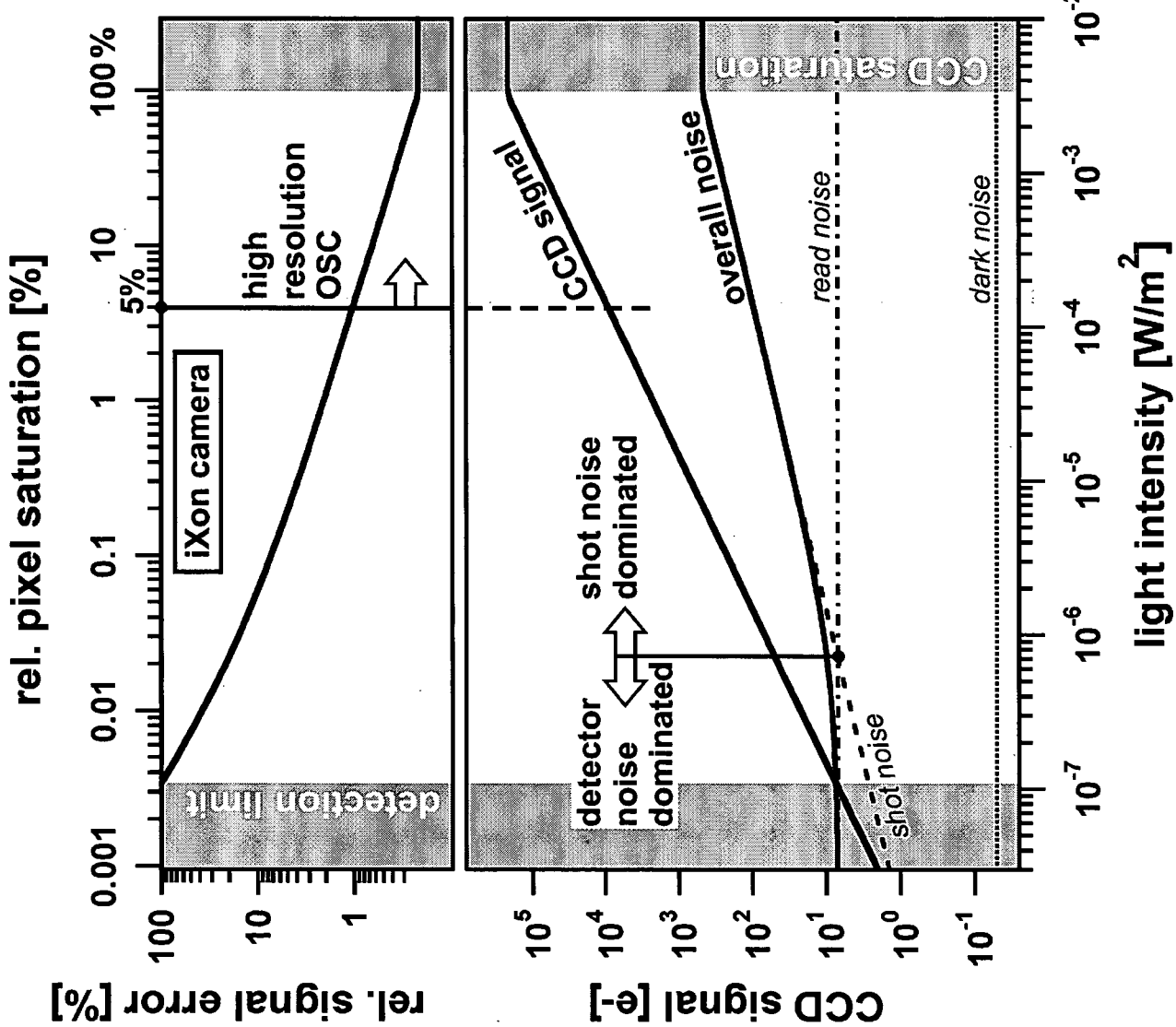
rel. pixel saturation [%]
0.001
0.01
0.1
1
5%
10
100 %
detection limit
iXon camera
high resolution OSC
rel. signal error [%]
100
10
1
CCD signal [e-]
10^5
10^4
10^3
10^2
10^1
10^0
10^{-1}
detector noise dominated
shot noise dominated
CCD signal
overall noise
read noise
dark noise
shot noise
CCD saturation
10^{-7}
10^{-6}
10^{-5}
10^{-4}
10^{-3}
10^{-2}
light intensity [W/m^2]

Fig. 10

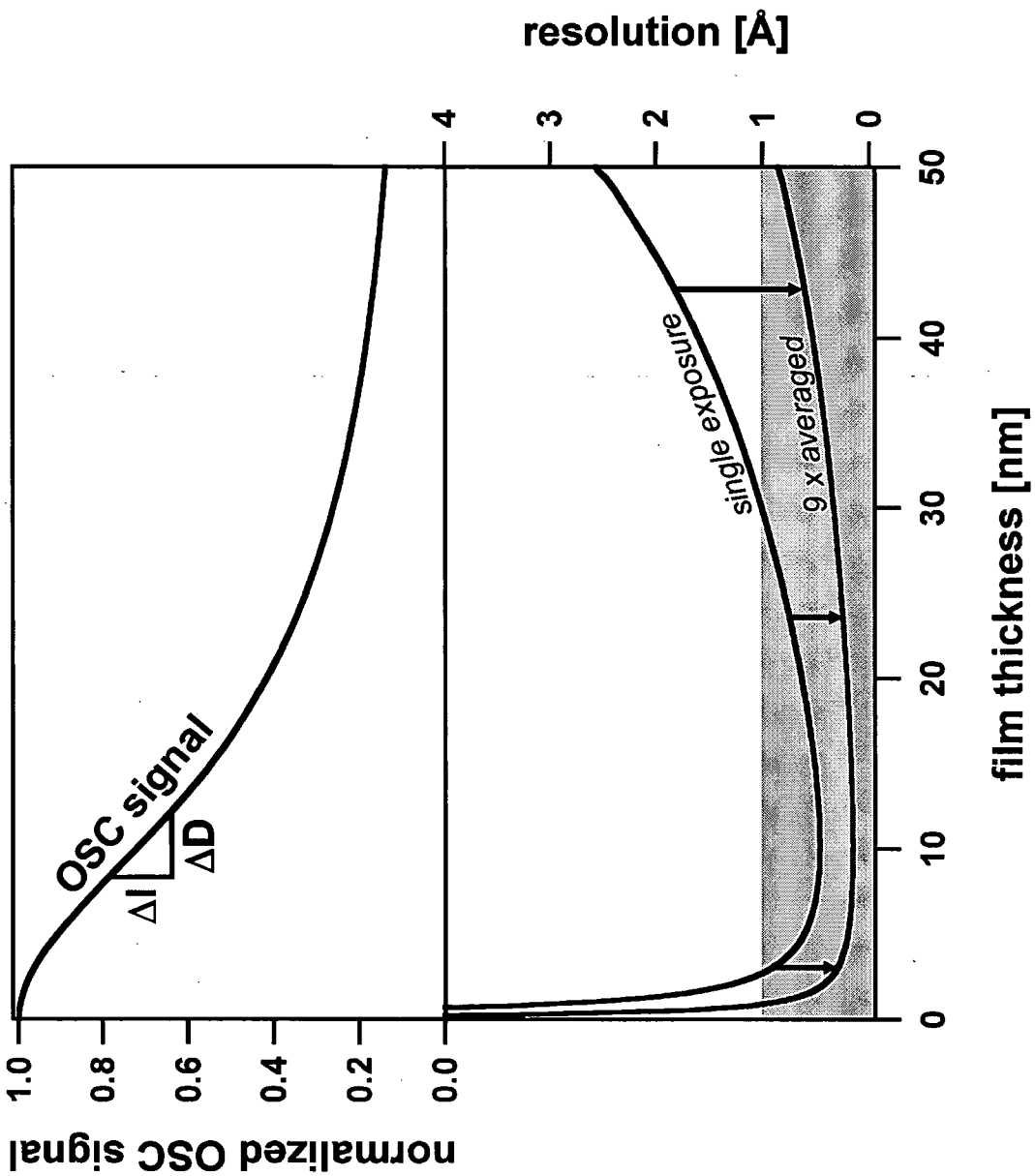
resolution [Å]
4
3
2
1
0
50
40
30
20
10
0
film thickness [nm]
single exposure
9 x averaged
OSC signal
ΔI
ΔD
1.0
0.8
0.6
0.4
0.2
0.0
normalized OSC signal

Fig. 11

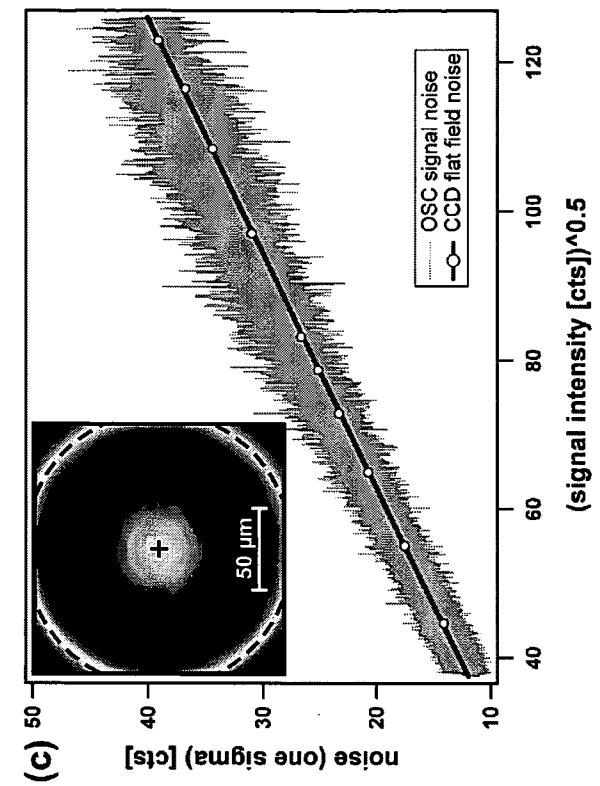
(c)
noise (one sigma) [cts]
(signal intensity [cts])^0.5
OSC signal noise
CCD flat field noise
50 µm

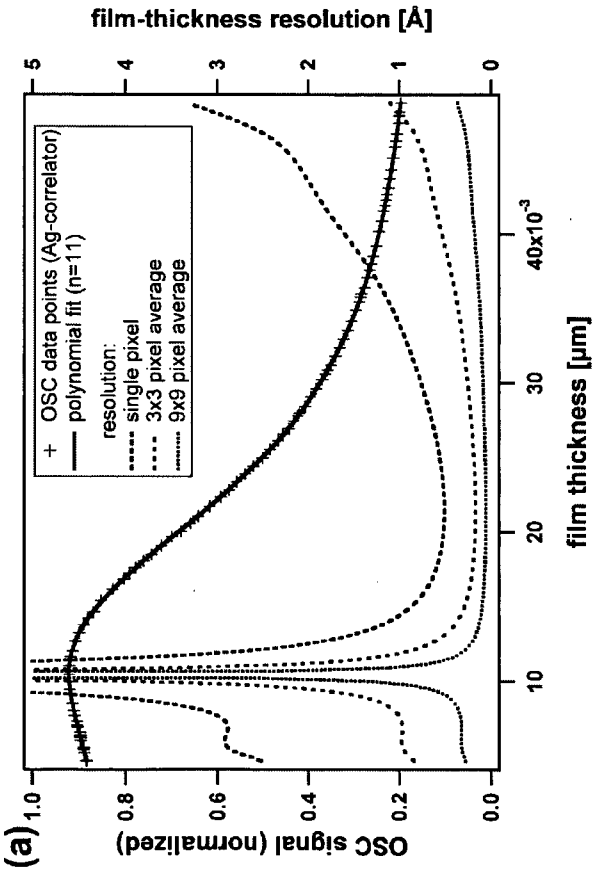
(a)
OSC signal (normalized)
film thickness [µm]
film-thickness resolution [Å]
OSC data points (Ag-correlator)
polynomial fit (n=11)
resolution:
single pixel
3x3 pixel average
9x9 pixel average

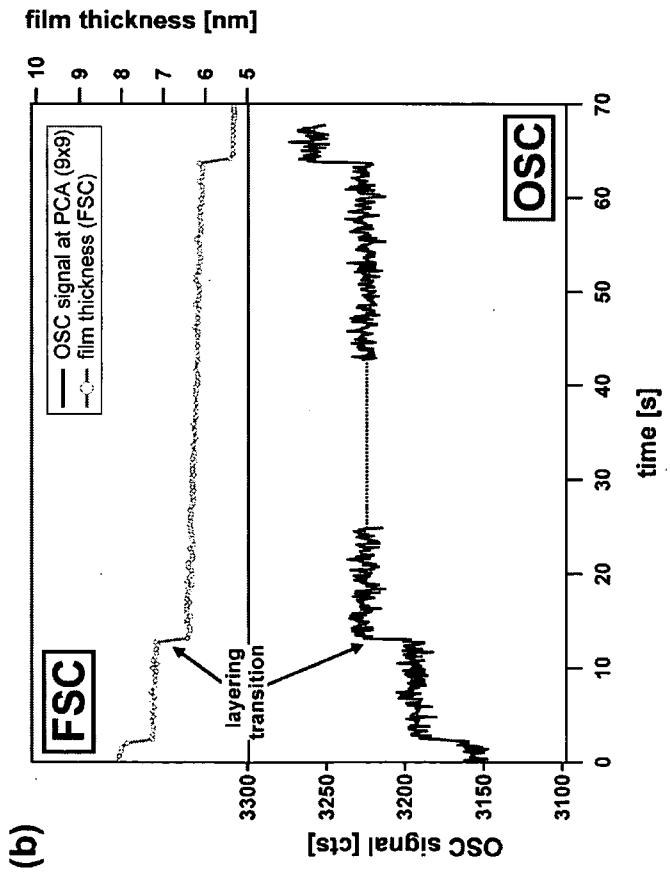
(b)
OSC signal [cts]
time [s]
film thickness [nm]
OSC signal at PCA (9x9)
film thickness (FSC)
FSC
OSC
layering transition

Fig. 12

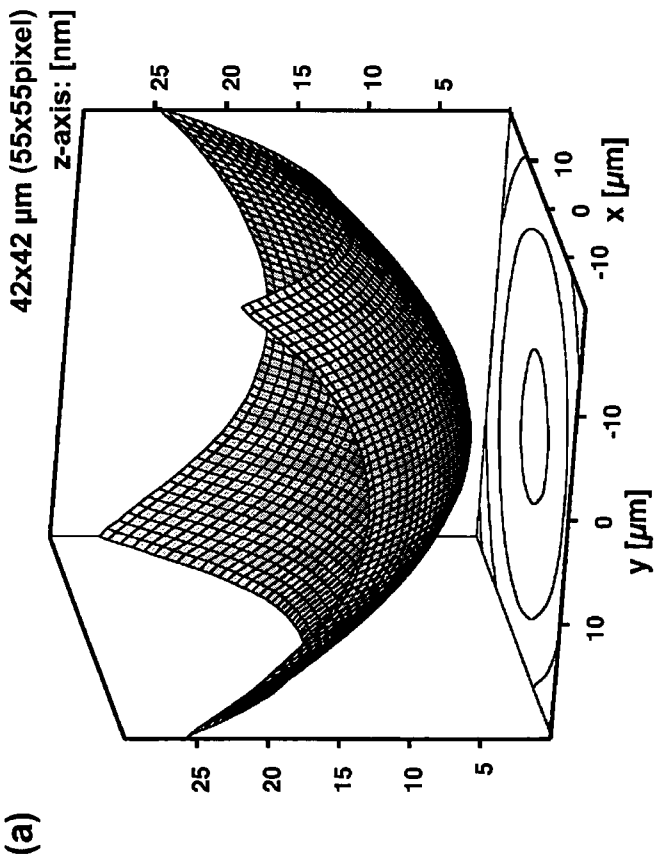
(a)
42x42 µm (55x55pixel)
z-axis: [nm]
25
20
15
10
5
x [µm]
y [µm]

Fig. 13

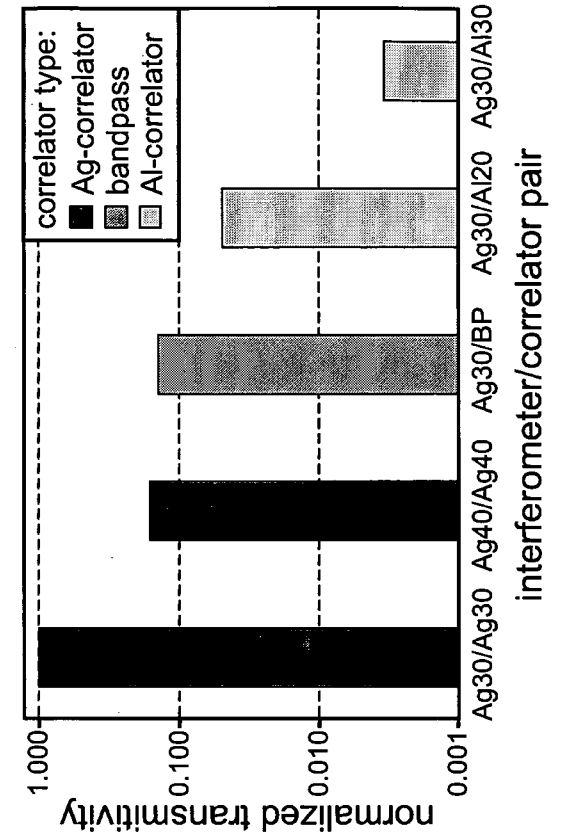
correlator type:
Ag-correlator
bandpass
Al-correlator
normalized transmitivity
1.000
0.100
0.010
0.001
Ag30/Ag30
Ag40/Ag40
Ag30/BP
Ag30/Al20
Ag30/Al30
interferometer/correlator pair

Fig. 14

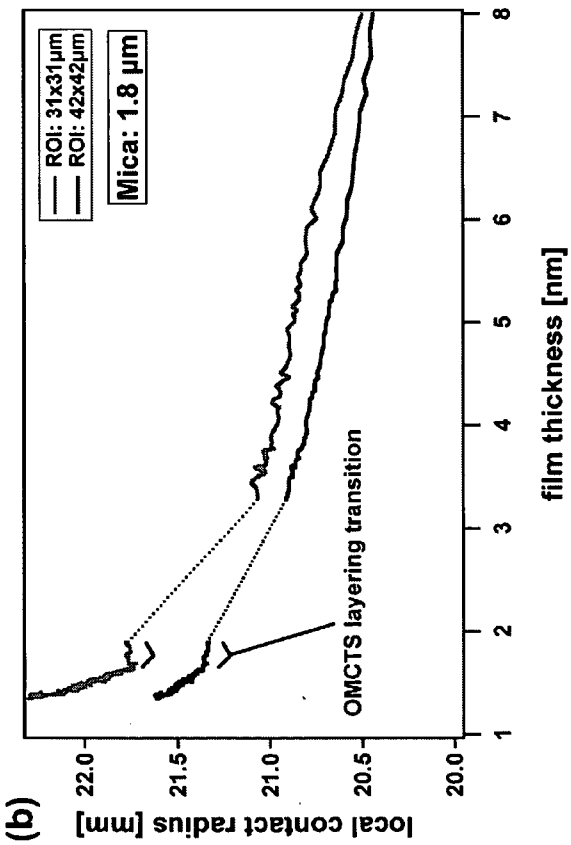
(b)
ROI: 31x31µm
ROI: 42x42µm
Mica: 1.8 µm
OMCTS layering transition
local contact radius [nm]
22.0
21.5
21.0
20.5
20.0
1
2
3
4
5
6
7
8
film thickness [nm]

Fig 15: List of major characteristics for a selection of biosensor types

	SPR	CPWR	SAR	OWLS	WIOS	Ellipso-meter	Rifs	TInAS
sensitivity [ng/cm^2]	0.1	10	10	0.5	0.2	1-5	1.0	1
sampling rate [Hz]	0.1-1	0.1	0.1-1	0.1	1-100	0.1	0.1	1-100
physical principle	evanescent plasmon excitation	plasmon-waveguide resonance	coherent, incoherent, reflection	grating waveguide coupling	grating waveguide coupling	reflection of polarized light	reflection Fabry-Pérot interferometry	transmission Fabry-Pérot interferometry
detection principle	goniometric photometric	photometric	goniometric photometric	goniometric photometric	spectro-metric photometric	polarization photometric	chromo-metric	spectro-metric photometric
substrate	metallic	dielectric multilayer, metallic	reflecting surface	dielectric waveguide	dielectric waveguide, transparent	reflecting surface	dielectric multilayer	transparent dielectric multilayer
optical quantity measured	ε_{eff}	ε_{eff}	n_{eff}, D, ...	n_{eff}, D, ...	n_{eff}, n_C, D, ...	n, D	D_{ads}	D_{ads}
wavelength range	IR	IR	vis	vis	vis / IR	vis	vis	vis
imaging capability	2D	-		1D	1D / 2D	-	-	2D

SUBSTITUTE SHEET (RULE 26)

INTERNATIONAL SEARCH REPORT

International application No
PCT/CH2008/000178

A. CLASSIFICATION OF SUBJECT MATTER
INV. G01N21/31 G01N21/45

According to International Patent Classification (IPC) or to both national classification and IPC

B. FIELDS SEARCHED

Minimum documentation searched (classification system followed by classification symbols)
G01N

Documentation searched other than minimum documentation to the extent that such documents are included in the fields searched

Electronic data base consulted during the international search (name of data base and, where practical, search terms used)
EPO-Internal, PAJ, WPI Data

C. DOCUMENTS CONSIDERED TO BE RELEVANT

Category*	Citation of document, with indication, where appropriate, of the relevant passages	Relevant to claim No.
Y	US 2003/190673 A1 (NIKITIN PETR IVANOVICH [RU] ET AL) 9 October 2003 (2003-10-09)	1,12
A	paragraph [0094] paragraph [0279] - paragraph [0290] paragraph [0325]	4-6,10, 14,16,17
Y	WO 00/23793 A (IMATION CORP [US]) 27 April 2000 (2000-04-27) page 6, line 3 - page 10, line 14; figure 3	1,12
A	DE 42 00 088 A1 (NAHM WERNER [DE]; BIOCHEM WISSENSCHAFTLICHE GERA [DE]) 15 July 1993 (1993-07-15) column 4, line 3 - column 5, line 11; claims 1-6	1,12

-/--

[X] Further documents are listed in the continuation of Box C.

[X] See patent family annex.

* Special categories of cited documents :

"A" document defining the general state of the art which is not considered to be of particular relevance

"E" earlier document but published on or after the international filing date

"L" document which may throw doubts on priority claim(s) or which is cited to establish the publication date of another citation or other special reason (as specified)

"O" document referring to an oral disclosure, use, exhibition or other means

"P" document published prior to the international filing date but later than the priority date claimed

"T" later document published after the international filing date or priority date and not in conflict with the application but cited to understand the principle or theory underlying the invention

"X" document of particular relevance; the claimed invention cannot be considered novel or cannot be considered to involve an inventive step when the document is taken alone

"Y" document of particular relevance; the claimed invention cannot be considered to involve an inventive step when the document is combined with one or more other such documents, such combination being obvious to a person skilled in the art.

"&" document member of the same patent family

Date of the actual completion of the international search	Date of mailing of the international search report
22 July 2008	28/07/2008

Name and mailing address of the ISA/	Authorized officer
European Patent Office, P.B. 5818 Patentlaan 2 NL - 2280 HV Rijswijk Tel. (+31-70) 340-2040, Tx. 31 651 epo nl, Fax: (+31-70) 340-3016	Stübner, Benno

INTERNATIONAL SEARCH REPORT

International application No
PCT/CH2008/000178

C(Continuation). DOCUMENTS CONSIDERED TO BE RELEVANT

Category*	Citation of document, with indication, where appropriate, of the relevant passages	Relevant to claim No.
A	US 2003/081875 A1 (KOCHERGIN VLADIMIR [US] ET AL) 1 May 2003 (2003-05-01) paragraph [0035] - paragraph [0041]; figure 1	1,12
A	GB 720 333 A (ERNST LEITZ GES MIT BESCHRAENK) 15 December 1954 (1954-12-15) page 3, line 6 - line 40; claims 1-3	1,12

INTERNATIONAL SEARCH REPORT

Information on patent family members

International application No
PCT/CH2008/000178

Patent document cited in search report	Publication date	Patent family member(s)	Publication date
US 2003190673 A1	09-10-2003	AU 6445101 A	26-11-2001
		EP 1288662 A1	05-03-2003
		WO 0188536 A1	22-11-2001
		RU 2181487 C2	20-04-2002
WO 0023793 A	27-04-2000	DE 69915851 D1	29-04-2004
		DE 69915851 T2	17-03-2005
		EP 1121583 A1	08-08-2001
		JP 2002527771 T	27-08-2002
		US 6320991 B1	20-11-2001
		US 2002018610 A1	14-02-2002
DE 4200088 A1	15-07-1993	NONE	
US 2003081875 A1	01-05-2003	EP 1444758 A1	11-08-2004
		JP 2005508095 T	24-03-2005
		WO 03038953 A1	08-05-2003
		US 2004202399 A1	14-10-2004
GB 720333 A	15-12-1954	NONE	